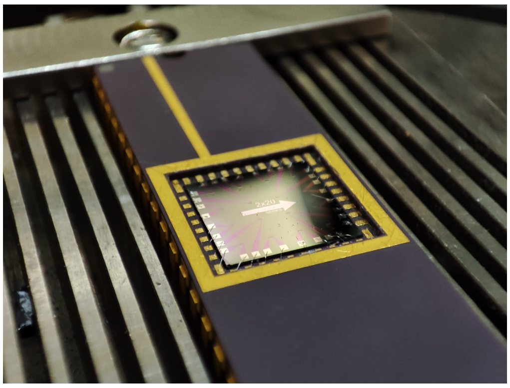

Towards a distributed magnetic tactile sensor network for flexible skin

Nuno Martinho dos Santos Lopes

Thesis to obtain the Master of Science Degree in

Engineering Physics

Supervisor(s):	Prof. Susana Isabel Pinheiro Cardoso de Freitas
	Prof. Alexandre José Malheiro Bernardino

Examination Committee

Chairperson: Prof. Carlos Manuel Dos Santos Rodrigues da Cruz
Supervisor: Prof. Susana Isabel Pinheiro Cardoso de Freitas
Member of the Committee: Prof. Diogo Miguel Bárbara Coroas Prista Caetano

November 2021

Dedicated to my family, Dani and the supermanos.

Acknowledgments

First, I would like to thank my supervisor, professor Susana Freitas for all the guidance and introducing me to this project and allowing and trusting in me to use any equipment in the INESC-MN facilities.

I would also like to thank my supervisor, professor Alexandre Bernardino, for his help and the discussions had during the project.

A special thanks to Pedro Ribeiro, who was truly a mentor, a huge help and a big part of me being able to finish this degree. Also to Miguel Neto for all the pointers given, the ideas discussed and helpful conversations we had.

For the uniaxial tensile tests, I have to thank professor Beatriz Silva for taking some of her time and helping me perform the tests. Also to professor Laura Pereira for her availability in receiving us in the CTN campus and helping us perform the SQUID measurements.

To Rita Pagaimo, who was my partner during a big part of my thesis, a big thank you for all the help with the stage and programming and also to Fabian Naff for the electronics acquisition board used in the sensor.

Also, I couldn't forget to thank Maria, Pedro, Jorge, Marília, Sara and all the others at INESC for their availability to help at any time and for making my time here the best I could've hoped for.

Finally the biggest thank you to my parents, girlfriend and friends, for putting up with me and supporting me through these 6 years.

Resumo

Os sensores táteis têm uma importância vital e cada vez maior em áreas como a robótica, com o objetivo de dar resposta às necessidades dos sistemas robóticos em adaptar-se a ambientes não estruturados.

Nesta tese, seguindo uma abordagem biomimética baseada na pele humana, um sensor tátil é desenvolvido que consiste numa matriz de 4×4 sensores de magnetorresistência de túnel (TMR) que detectam a variação de campo magnético causada pela aplicação de forças num elastómero magnetizado com o momento magnético definido na direção sensível dos sensores TMR. Além disso, também é estudada a influência de 4 configuraccões de magnetização do elastómero distintas na capacidade de deteção do sensor.

A capacidade dos sensores para detetar a intensidade da força e a sua localização é demonstrada usando-se para o efeito algoritmos de aprendizagem supervisionada. A intensidade de forças normais é estimada com um mínimo erro absoluto médio de aproximadament 0.023N e um máximo de 0.1N entre todas as 4 distintas configurações de magnetização. A capacidade de distinguir a localização de 5 diferentes pontos de aplicação da força foi também observada com uma precisão mínima de 97% entre as configurações de magnetização.

Um modelo de simulação também foi desenvolvido, capaz de determinar a resposta de elastómero magnetizado a uma força aplicada. Finalmente, os resultados deste modelo foram validados, comparando-os com dados obtidos experimentalmente.

Palavras-chave: Sensor de magnetorresistência de túnel, pele artificial, magnetização distribuída, sensor tátil

Abstract

Tactile sensors are of increasingly vital importance in fields such as robotics, to answer the needs of robotic systems in adapting to unstructured environments.

In this thesis, following a biomimetic approach based on human skin, a tactile sensor is developed consisting in a matrix of 4×4 TMR (tunnel magnetoresistive) sensors which detect the change in magnetic field in a magnetized elastomer, with the magnetic moment set to the TMR sensors' sensitive direction, when it is actuated by a force. It is also studied the influence of 4 different elastomer magnetization configurations.

The sensors' ability to detect force intensity and location is demonstrated by using supervised learning algorithms. The intensity of normal forces is estimated with a minimum mean absolute error of approximately 0.023N and a maximum of 0.1N among different magnetization configurations. The ability of differentiating the location of 5 different application points of the force was also observed with a minimum accuracy of 97% among the magnetization configurations.

A simulation model was also devised which was able to determine the response of magnetized elastomer to an applied force. Finally, the results of this model were validated against obtained experimental data.

Keywords: Tunnel Magnetoresistive sensor, flexible skin, distributed magnetization, tactile sensor

Contents

List of Tables

List of Figures

Nomenclature

AFM	Antiferromagnetic
AMR	Anisotropic Magnetoresistance
DWL	Direct Write Laser
FEM	Finite Element Method
FM	Ferromagnetic
GMR	Giant Magnetoresistance
IBD	Ion Beam Deposition
IBM	Ion Beam Milling
MP	Magnetic Particle
MR	Magnetoresistance
MTJ	Magnetic Tunnel Junction
PECVD	Plasma Enhanced Physical Vapour Deposition
PWM	Pulse Width Modulation
RF	Radio Frequency
RIE	Reactive ion etching.
SAF	Synthetic Antiferromagnet.
SVG	Silicon Valley Group
TMR	Tunnel Magnetoresistance
UHV	Ultra High Vacuum

Chapter 1

Introduction

1.1 Motivation and objectives

As the field of robotics evolves, tactile sensing's role in this area also gains increased importance. The environment with which robots interact is often times unstructured and the demand is high for technologies that, by helping robots gain an increased perception of their surroundings, can help make these interactions safer whether they are with objects or humans [1].

To help materialize this objective, a biomimetic approach is often followed by researchers which results in the development of different technologies such as cilia [2] or artificial skins [3] that can mimic structures with the same purpose already found in nature and, in particular, humans.

Moreover, research and development of magnetoresistive sensors has seen tremendous advances in the last decades. In particular tunnel magnetoresistance sensors could be used to increase the sensitivity of tactile sensors.

Although there is not a definition of characteristics these tactile technologies should possess, they should be able to detect forces, with high sensitivity and wide range and in a wide contact area. They should also be simple to avoid complex electronics and bulky data processing centers.

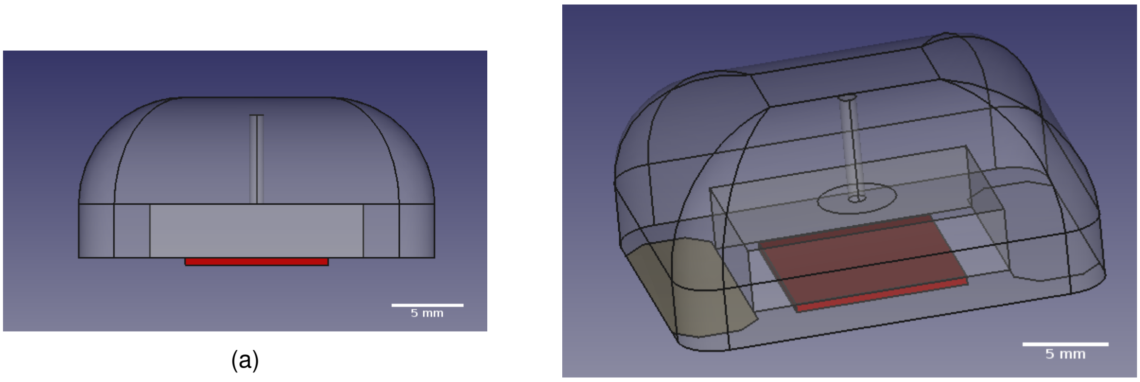

(a)

(b)

Figure 1.1: Design of the tactile sensor developed in this thesis. In red is represented the TMR sensor die and in grey the *EcoFlex* piece.

As such, in this work a force sensor is developed, capable of detecting small forces by deformation of a magnetised elastomer-based artificial skin.

The sensor is composed of an artificial elastomer-based magnetized skin structure placed on top of a 4x4 array of 1-dimensional sensing TMR sensor (as shown in Figure 1.1) that detects the changing direction of the free layer's magnetization due to variations in the external magnetic field caused by deformations in the artificial skin when forces are applied. These forces can be associated to the change in resistivity measured at the output of the sensors.

So, the main goals of this work will consist in:

- Development of a tactile sensor consisting of an array of TMR sensors with the same sensitive direction and magnetized elastomer structures who act as the source of the stray field;

- Simulation of the elastomer-based artificial skin deformation and magnetic field expected at sensors positions, hence sensors output expected;

- Characterization of tactile sensor output with applied force and contact position;

1.2 Chapter summary

In what's left of chapter 1 a review of the state of the art is made on existing tactile sensing technologies and artificial skin.

In chapter 2 a theoretical introduction to the topics and physical models used in the development of the sensor: magnetostatics, material deformation and TMR effect and magnetic tunnel junctions.

In chapter 3 a description is given of the fabrication and characterization methods used. The TMR sensors fabrication process is detailed, including steps and systems/machines used. The fabrication of the elastomer pieces is also described as well as its characterization.

Chapter 4 describes the process of renovating and programming a 3D precision movement stage that happened out of a need for a platform for precision movement to use in the force test setup. Dimensioning and building, electrical connections and Arduino programming of the stage are covered in this chapter

In chapter 5 the models for the simulations made for the system in development are described. The simulation models, parameters, conditions, etc are reported.

Experimental tests are made on the sensors. The respective results are detailed and analysed, using supervised learning algorithms, in chapter 6. The characterization of the sensors is made.

This thesis is concluded in chapter 7 with a summary of the work done, results achieved and perspectives on future work.

1.3 State of the art

1.3.1 Tactile sensing technologies

The main technologies for tactile sensing are based in capacitive, piezoresistive, piezoelectric, magnetic and optical methods, these will be shortly described below and Table 1.1 presents a summary of advantages and disadvantages of several technologies.

Capacitive: capacitive tactile sensors are composed of 2 conductive plates (electrodes) with a layer of dielectric material between them. They take advantage of the change in capacitance when a force is applied. The capacitance of a parallel plate capacitor is given by $C = \epsilon_0 \epsilon_r \frac{A}{d}$. Where ϵ_0 is the vacuum permittivity, ϵ_r is the dielectric layer's relative permittivity, d is the distance between electrode plates, and A is the area in which both electrodes overlap. One can measure the force applied on the sensor by tracking the changes either in A or d [4].

They usually show good frequency response, high sensitivity and large dynamic range, making them appealing to researchers, however they are more prone to noise (crosstalk) which requires complex electronics to filter [5][6].

Piezoelectric: piezoelectric sensors active components are materials, that generate a voltage potential proportional to the deforming external forces (called piezoelectric materials). Piezoelectric sensors measure these voltage variations. The tactile element is constructed by applying thin layers of metal to both sides of the piezoelectric material, turning it into a parallel plate capacitor. They generally have a good high-frequency response with high sensitivity in dynamic environments. However, due to the quick dissipation of the charge induced on the piezoelectric material, they are unable to measure static forces only being able of detecting dynamic forces due to their large internal resistance [6][7].

	Advantages	**Disadvantages**
Capacitive	High sensitivity High spacial resolution Good dynamic range Independence of temperature	Susceptible to noise Stray capacitance Crosstalk
Piezoresistive	High spatial resolution Low susceptibility to noise Simple electronics	Hysteresis High power consumption Low repeatibility
Piezoelectric	High frequency response High dynamic range High sensitivity	Poor spatial resolution Only dynamic sensing
Magnetic	Linear output High spatial resolution High sensitivity	Crosstalk Low frequency response Complex electronics
Optical	Immunity to EMI Large sensing range High repeatability High spatial resolution	Bulky Non-conformable Processing power requirements

Table 1.1: Relative advantages and disadvantages of tactile transduction techniques

Piezoresistive: tactile sensors employing this transduction technique work by changing the electrical resistance of a material placed between or in touch with 2 electrodes when an external force is applied.

The electronic data acquisition setup for these sensors is usually a simple one, as a change in resistance is easy to quantify by the Ohm's law. They obtain good results in mesh configurations due to their low susceptibility to noise. However, this type of sensors suffer from hysteresis and low frequency response and their behaviour tends to be susceptible to humidity and temperature changes[8] [9].

Optical: Optical tactile sensors work by measuring changes in light. Usually, optical fibers are used as the transmission medium for light. When an external force is applied the transmitting medium (optical fibers) is bent and such sensors can, for example, measure the change in light intensity at the output using a camera or a photodiode. Advantages of these sensors include light weight, immunity to electromagnetic phenomenons and high spatial resolution. However, they require a lot of processing power and their rigidness and bulk is a major disadvantage [6][10].

Magnetic: Magnetic tactile sensors measure changes in the magnetic field generated by a permanent magnet in the vicinity of the sensors. When a force causes a displacement of the magnet and hence of the magnetic field, this MF variation will lead to a voltage difference at the output of the sensor, that can be measured and used to deduce the force. These can be Hall effect sensors [11], magnetoimpedance [12] or magnetoresistance based. They present high resolution and high sensitivity however, when compared to other kinds of sensors, they are power consuming, require more complex electronics and are prone to stray capacitance.

Magnetoresistance is the property of a material to change its resistance according to an applied external magnetic field. This change happens because of an existing dependence of the resistance of said material with the direction of the magnetization. The Magnetoresistance can be expressed by the following ratio:

$$MR(\%) = \frac{R_{min} - R_{max}}{R_{min}} \times 100 \tag{1.1}$$

The values of R_{min} and R_{max} for a material can be obtained by sweeping the magnetic field applied to it while measuring the resistance.

Various effects are observed that have a basis in magnetoresistance, and some of them with applications in magnetic sensors, such as the Anisotropic Magnetoresistance (AMR) effect, the Giant Magnetoresistance (GMR) effect and the Tunnel Magnetoresistance (TMR) effect, which is the relevant one for this work. While in the anisotropic magnetoresistance effect the resistivity varies with the angle between the magnetization and the material easy axis, in the giant and tunnel magnetoresistance effects the value of resistivity is changed on a non-magnetic (GMR) conductive barrier or an insulating barrier (TMR) when the relative orientation between the magnetization of layers of ferromagnetic material is changed by an external field. Due to their high sensitivity when compared to the others, TMR based sensors were chosen to be used in this work.

1.3.2 Artificial skin

As referenced before, one can have a biomimetic approach to the development of tactile sensing technologies, finding inspiration in nature for features of sensors. In the case of artificial skin, the principal source of inspiration is, of course, the human skin.

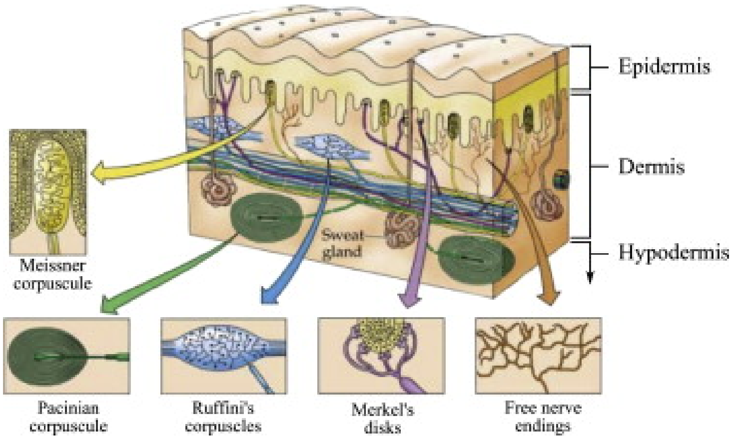

Figure 1.2: Mechanoreceptors present in hairless (glabrous) skin. [13]

The human skin has several kinds of mechanoreceptors, capable of tactile sensing. Ruffini endings, for example, are located in the dermis and respond to pressure and stretch on skin, while Merkel disks are located in the epidermis and respond to pressure, texture and spatial deformations. Both of these mechanoreceptors are slow adaptors (SA), which means they send constant response to constant stimuli, hence are able to sense static forces [14]. On the other hand, Meissner's corpuscules are located in the dermis and respond well to dynamic skin deformation such as vibrations, while the Pacinian corpuscules can be found in the deep layers of the dermis and are particularly sensitive to high frequency stimuli and small deformation of skin. Both of these are rapid adaptors (RA) meaning that they have primarily dynamic response [13]. These mechanoreceptors are located primarily in glabrous skin, such as in the fingertips as shown in Figure 1.2.

Artificial skin technologies for force/pressure sensing have been developed, mainly consisting of a transduction medium embedded in a rubber-like material, such as the corpuscles "embedded" in the skin sense forces. One of the recent developments in magnetic artificial skin is to use elastomers embedded with magnetic particles. Although there is not a set of mandatory characteristics to possess, human skin-like tactile sensors should be able to have a spacial resolution of about 1-2mm, a sensitivity of about 0.01 Newton and a range of 10 Newton and they should also be robust and have high repeatability [14].

Technologies such as these have been described using each of the transduction technologies talked about in 1.3.1: piezoresistive [15], capacitive [16], piezoelectric [17], optical [18] and magnetic [19],[20].

One of the recent developments in magnetic artificial skin is to use elastomers embedded with magnetic particles, as the elastomer is deformed by applied forces, the magnetic field generated by the particles is changed and this is detected by sensor.

Such an artificial skin is presented by Yan et al [19]. In that work a prototype of sensor is presented using an artificial magnetic skin composed of a Hall sensor embedded in a layer of *EcoFlex* and a thin layer of sinusoidally magnetized PDMS film on top. The deformation of this film leads to changes in the magnetic flux densities which are measured by the Hall effect sensor. The sensor was able to accurately measure normal and shear forces with a single unit and achieves super-resolved accuracy by deep-learning methods.

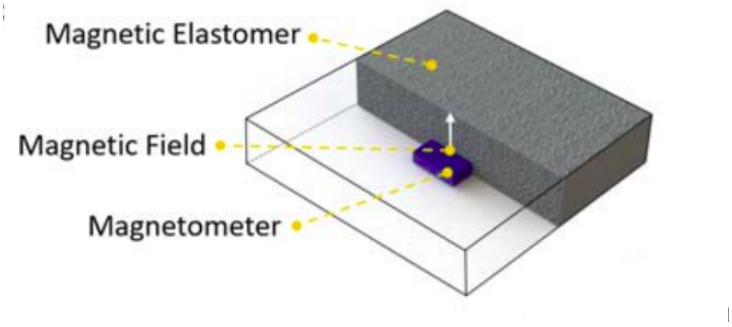

Figure 1.3: Magnetized artificial skin sensor presented in [20]

Another example of magnetic particle-embedded elastomeric artificial skin is reported by T. Hellebrekers et al [20] that consisted in an elastomer embedded with Ne-Fe-B particles that are on the order of $\approx 200\mu m$ in diameter. The change in the magnetic field is detected by a 3-axis magnetometer (Figure 1.3). The advantage of this method is that the elastomer can be doped with high concentrations of magnetic particles, and sensing can be done in a continuous area. Using machine learning based techniques the raw magnetic data is used to determine the intensity and location of the external force. Using quadratic discrimination analysis algorithms it was possible to distinguish between 25 grid locations in a 15 mm^2 area with ¿98% accuracy and regression algorithms can localize contact to a 3 mm^2 area within the 15 mm^2 active sensing area. Force intensity was also estimated using a k-nearest neighbours regression, with a mean error ranging from 0.25- 0.44 N depending on the experiment.

Chapter 2

Theoretical Background

This chapter functions as a theoretical introduction to the main subjects in this dissertation, needed for a better understanding of the principles behind the functioning of the magnetoresistive tactile sensor developed. A brief introduction to topics of magnetostatics is given, to help better understand the structures, embedded in the *EcoFlex*, that are the source of the stray magnetic field detected by the sensor. This is followed by a description on the working principles and theory behind magnetic tunnel junctions. Finally, an introduction to the deformation of hyperelastic materials is given to help create a basis for understanding the deformation of the *EcoFlex* pieces.

2.1 Magnetostatics

Consider Maxwell's equation for the magnetic flux density **B**, which states that the magnetic flux density's divergence is 0 [21]:

$$\nabla \cdot \mathbf{B} = 0 \tag{2.1}$$

And also Maxwell's equation for the magnetic field **H**:

$$\nabla \times \mathbf{H} = \mathbf{J} \tag{2.2}$$

The magnetic flux density and magnetic field relate to each other through the following equation:

$$\mathbf{B} = \mu_0(\mathbf{H} + \mathbf{M}) \tag{2.3}$$

with $\mu_0 = 4\pi \times 10^{-7} H/m$ being the vacuum permeability and **M** the magnetization. Combining equations 2.1 and 2.3, one is left with:

$$\nabla \cdot \mathbf{H} = -\nabla \cdot \mathbf{M} \tag{2.4}$$

The parallel can be made between magnetic field in this approach and the electric field in electrostatics, where it arises from a distribution of magnetic charges q_m and the field created by a single charge would be $H = \frac{q_m \mathbf{r}}{4\pi r^3}$. These magnetic charges, unlike the electric charges, have no physical meaning being only useful as mathematical tools - what is observed in reality are magnetic dipoles.

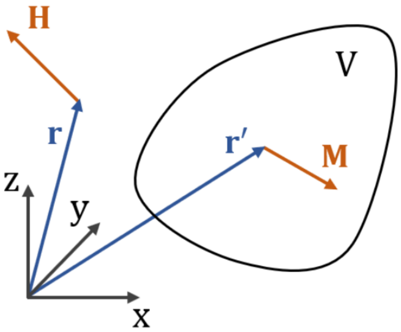

Figure 2.1: Scheme of the geometry for the integration of equation 2.4. (Taken from [22]).

Then, the magnetic field at an arbitrary point with position vector **r** in space, generated by some magnetized volume (V) (as shown in Figure 2.1) through the surface S, can be calculated by:

$$\mathbf{H}(\mathbf{r}) = \frac{1}{4\pi}\left\{ -\int_V (\nabla \cdot \mathbf{M}(\mathbf{r'}))\frac{\mathbf{r}-\mathbf{r'}}{|\mathbf{r}-\mathbf{r'}|^3}\, d^3r' + \int_S (\mathbf{M}(\mathbf{r'}) \cdot \mathbf{e}_n)\frac{\mathbf{r}-\mathbf{r'}}{|\mathbf{r}-\mathbf{r'}|^3}\, d^2r' \right\} \tag{2.5}$$

in this expression **r'** is the position vector for the infinitesimal charge being considered and $\mathbf{e}_n$ is the surface normal unit vector at **r'**. This equation can be used as a starting point for the calculation of the external magnetic field generated by both the permanent magnets and the magnetized *EcoFlex* over the magnetoresistive sensors.

2.2 TMR effect and Magnetic tunnel junctions

2.2.1 The TMR effect

The TMR effect was first proposed by Julliere in 1975 [23] to explain the tunneling of electrons from one ferromagnetic (FM) layer to another through a sufficiently thin insulating barrier (the simplest form of a MTJ structure) when a voltage is applied between the 2 FM layers.

The two main assumptions made in Julliere's model are:

- The conservation of spin of the tunnelling electrons, which means that spin up electrons can only tunnel between the two FM layers to spin up states and spin down electrons to spin down states;

- The tunnelling probability is proportional to the product between the density of states in the electrons' FM layer of origin and the one where he tunnels to.

Hence, the current density for the parallel (J_P) and anti parallel (J_{AP}) configurations of the ferromagnetic layers of the MTJ are given by the expressions below, where $D_i(\uparrow / \downarrow)$, $i = 1, 2$ represent the density of spin up or down states for the ferromagnetic layer i at the Fermi level (only these ones contribute to conduction).

$$\begin{aligned} J_P &\propto D_1(\uparrow)D_2(\uparrow) + D_1(\downarrow)D_2(\downarrow) \\ J_{AP} &\propto D_1(\uparrow)D_2(\downarrow) + D_1(\downarrow)D_2(\uparrow) \end{aligned} \tag{2.6}$$

The TMR effect in MTJs then originates from an existent difference between the density of spin up and spin down states in ferromagnetic materials at the Fermi level. This imbalance leads to the aforementioned spin-dependent tunelling of electrons. This will lead to the dependence of the TMR(%) ratio on the relative direction of the magnetization of both ferromagnetic layers and their spin polarization, as depicted by Figure 2.2, in the following manner:

$$TMR(\%) = \frac{R_{min} - R_{max}}{R_{min}} \times 100 = \frac{R_{AP} - R_P}{R_P} \times 100 = \frac{2P_1P_2}{1 - P_1P_2} \times 100 \tag{2.7}$$

Where R_{AP} corresponds to the resistance measured for the anti parallel relative orientation of the magnetization of the ferromagnetic layers, which will be the maximum resistance possible for the structure at hand, and R_P is the minimum resistance, corresponding to the parallel orientation of the magnetization. In this expression the polarization factors P_1 and P_2, of the ferromagnetic layers are given by

$$P = \frac{D(\uparrow) - D(\downarrow)}{D(\uparrow) + D(\downarrow)} \tag{2.8}$$

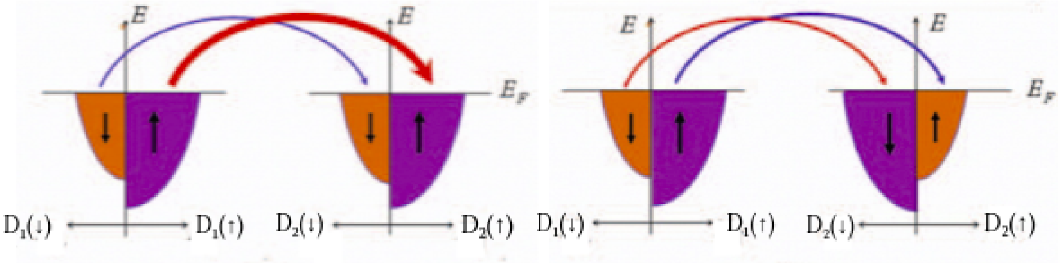

Figure 2.2: Schematic of density of states and spin dependent tunneling of electrons for the parallel configuration (left) and the anti parallel configuration (right) of the magnetization of ferromagnetic layers (adapted from [24]).

2.2.2 Magnetic Tunnel Junctions

As mentioned before, a MTJ in its most basic form is comprised of only a thin insulating barrier layer, usually AlO$_x$ or MgO, sandwiched between two ferromagnetic layers. One of these layers is called the pinned layer, because of its fixed magnetization orientation, due to the exchange bias interaction with an adjacent anti-ferromagnetic (AFM) layer. While the other layer is called the free one, because its magnetization orientation changes with the application of even small external magnetic fields. In contrast, in order to be able to change the direction of the magnetization of the pinned layer, a very strong magnetic field would have to be applied.

Besides these layers, the usual MTJ structure is also composed of buffer layers on top and bottom and a capping layer on top. The buffer is usually made of dense, non-magnetic metals such as Ta and Ru in alternated layers and is useful to enhance electrical properties and to promote proper crystallographic growth [25]. The cap layer is also composed of a non-magnetic metal and ends the stack of an MTJ. It serves as protection against oxidation and etching for the layers below.

In the sensors used in this thesis, the pinned layer is replaced by a synthetic anti-ferromagnet (SAF) structure. These structures consist of two ferromagnetic layers separated by a thin spacer layer. The coupling of the two FM layers is described by the RKKY theory [26] and can be ferromagnetic or anti-ferromagnetic depending on the distance between them, i.e., the thickness of the spacer, as shown in Figure 2.3. The layer which is adjacent to the anti-ferromagnet is the pinned layer and the other one is the reference layer. The SAF structure is used in detriment of the single anti-ferromagnetic layer because it increases the exchange field (the value of magnetic field needed to reverse the direction of magnetization of the pinned layer) and it provides stability to the MTJ.

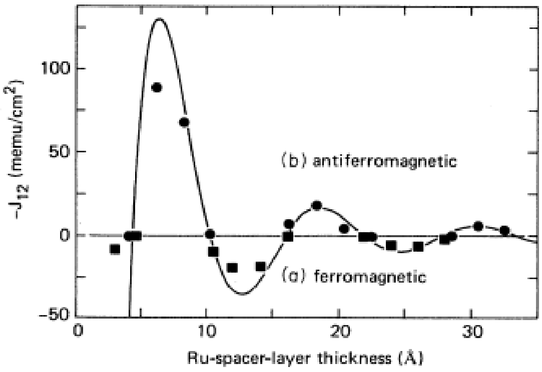

Figure 2.3: Coupling strenght of between two ferromagnetic layers as a function of the Ru spacer thickness [27].

Besides the SAF structure, a SFM (synthetic ferromagnetic) structure is also often used as a free layer, especially in MTJs with an MgO barrier. In such structures, such as in the case of this thesis, a soft magnet material such as NiFe is used adjacent to the CoFeB contributing to the low magnetic anisotropy of the free layer and reducing coercivity. A layer of a non-magnet material, Ru in this work, is also patterned between the two aforementioned layers for texture matching, since the NiFe does not adhere to the CoFeB strongly, and also for the 2 magnetic layers to ferromagnetically couple, allowing for high sensitivity in the MTJ [28]. A scheme of the stack deposited in this work is shown in Figure 3.1.

2.2.3 MTJ linearization strategies

Depending on the application, MTJs can be designed to have a hysteretic or a linear response, more appropriate for sensing applications. A linear response is achieved by making sure the relative direction of the easy axis of the free and pinned layers are orthogonal, in the absence of an external magnetic field. On the other hand an histeretic response is achieved by making sure this direction is parallel [29]. Figure 2.4 shows examples of both linear and hysteretic responses.

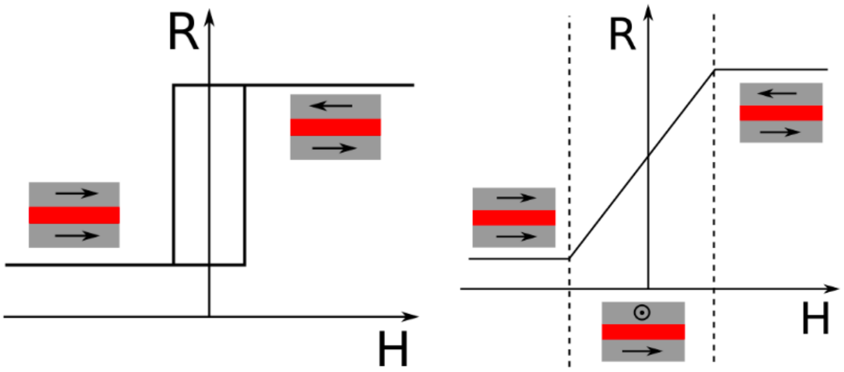

Figure 2.4: Transfer curves schematic for an MTJ: parallel anisotropies with hysteretic response (left) and orthogonal anisotropies with linear response (right). [30]

Since usually during the deposition of the stacks, the easy axes of both the pinned layer and the sensing layer are defined parallel to one another due to an intrinsic anisotropy created by the deposition in the presence of a constant magnetic field, there are several strategies to induce perpendicular anisotropy and therefore a linear response in MTJs, such as:

- Defining a crossed anisotropy by applying orthogonal magnetic fields during the deposition of the pinned and sensing layers (Figure 2.5 a));
- Using integrated permanent magnets or current lines as a way of creating a biasing external magnetic field (Figure 2.5 c));
- Reducing the sensing layer thickness until the superparamagnetic limit (Figure 2.5 d));
- By adding a soft-pinning antiferromagnetic layer adjacent to the sensing layer which, through exchange interaction, sets the magnetization on a fixed direction (Figure 2.5 e));
- Taking advantage of the self-demagnetizing field of the sensing layer which is created by controlling MTJ geometry, to set the anisotropy of the sensing layer perpendicular to the pinned layer (shape anisotropy) (Figure 2.5 b));

In this work, the linearization of the MTJs is achieved mainly by shape anisotropy. Since in a retangular shaped MTJ one has a free layer thickness much smaller than its width and height (W,h $\gg$ t), it is safe to assume that the layers magnetization is always in the sensor plane, as is its self-demagnetizing field. Under this assumption, we have from [31] the analytical solution for both components (width and height) of the self-demagnetizing field (H_d), as a function of the sensors dimensions (w,h,t), and the saturation magnetization (M_s):

$$\begin{cases} H_d^h = -\frac{8M_s}{4\pi}\frac{t}{\sqrt{w^2+h^2}}\frac{w}{h}cos\theta \\ H_d^w = -\frac{8M_s}{4\pi}\frac{t}{\sqrt{w^2+h^2}}\frac{h}{w}sin\theta \end{cases} \tag{2.9}$$

Assuming the easy axis of the pinned layer is along the height of the MTJ, the sensor can then be designed to have a large aspect ratio and, as mentioned before, take advantage of shape anisotropy.

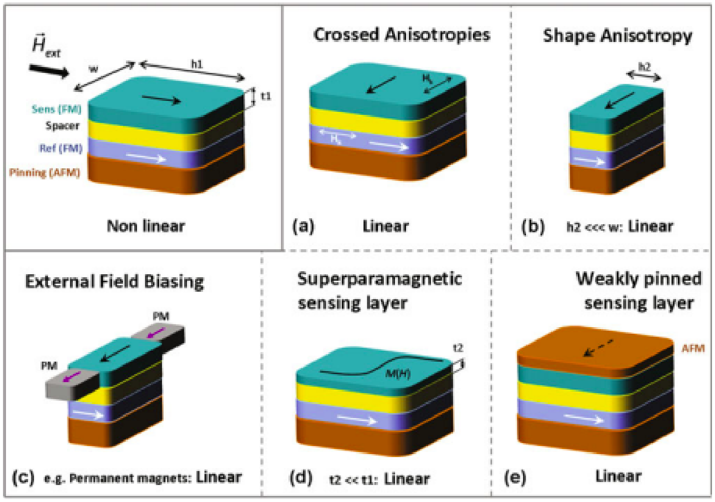

Figure 2.5: Linearization strategies schemes [25].

With a higher aspect ratio w:h (of the order of 10:1), it is possible to set the anisotropy of the sensing layer perpendicular to that of the reference layer, because the H_d^w becomes more dominant [25]. This increase in aspect ratio also leads to an increased linear range but a decreased sensitivity in consequence.

2.3 Material Deformation

The strain (ϵ) vs stress (σ) relation of a material is usually used to describe the deformation it suffers. The stress can be seen as the force which the material is under, that causes the deformation, and the strain expresses this deformation when the stress is applied.

In this thesis, the material under stress are the *EcoFlex* pieces, and they should be able to deform and return to their original position without suffering a permanent change of shape. This behaviour in which the deformation is reversible is called elastic behaviour. This is presented in a strain vs stress plot as a major region of interest in which the relation between the two variables is linear, and the slope is the Young modulus (E). The other important behaviour of materials under deformation is the plastic behaviour, where the deformation is not reversible, this is also presented in the strain vs stress plot, as can be seen in Figure 2.6.

As said before, the stress relates to the strain linearly by Hooke's law, as follows, where E is the Young modulus [32]:

$$E = \frac{\epsilon}{\sigma} \tag{2.10}$$

However, for rubber-like materials (as is the case of *EcoFlex*) the plastic behaviour region is virtually non-existent, as can be seen in Figure 2.6. These are called hyperelastic materials, they can be put under very large stresses and recover their original shape, not deforming permanently, which is why they are used in this work. For hyperelastic materials, the linear model presented before is not accurate, hence a strain energy density function W is used to describe them, that relates the strain energy density of the material to the deformation.

Several theories have been devised to explain the behaviour of hyperelastic materials, one of the most successful being the Generalized Rivlin Model (or polinomial hyperelastic material model), which is an empirical model where the strain energy density function is a polinomial that depends on the two invariants of the left Cauchy-Green deformation tensor I_1, I_2. For incompressible materials such as *EcoFlex*, this function is as follows [33]:

$$W = \sum_{i,j=0}^{n} C_{ij}(I_1 - 3)^i (I_2 - 3)^j \tag{2.11}$$

where C_{ij} are material constants with $C_{00} = 0$ and $I_1 = \lambda_x^2 + \lambda_y^2 + \lambda_z^2$, $I_2 = \lambda_x^2\lambda_y^2 + \lambda_y^2\lambda_z^2 + \lambda_z^2\lambda_x^2$. Here λ_i are the principal stretch ratios at the point considered.

These theories are relevant in that they provide a theoretical framework for the understanding of the deformation of the elastomer used in this work, and consequently the simulation models subsequently devised.

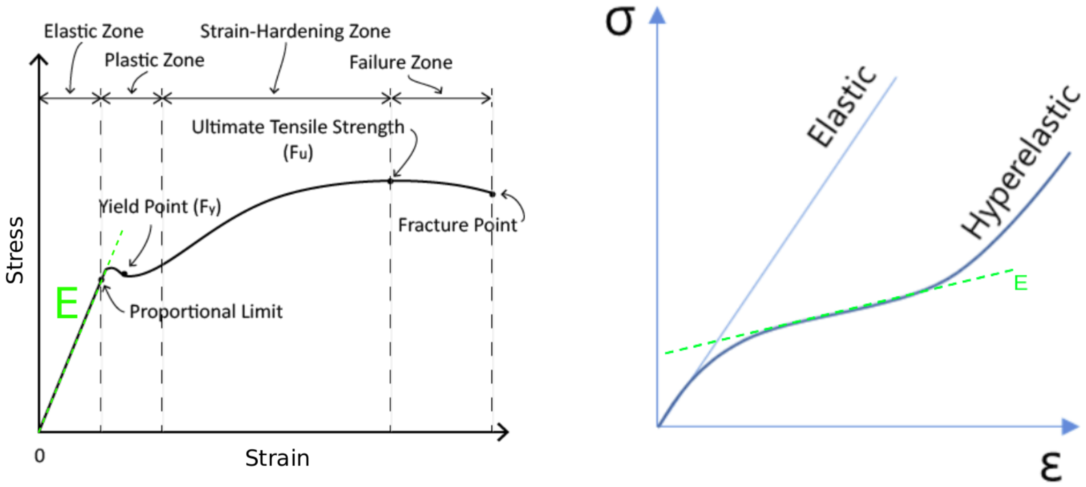

Figure 2.6: Strain vs stress curves. On the left the typical curve of a material like steel with the several phases experimented by steel for different strains (taken from [30]). On the right the curve for a hyperelastic material. The dashed line represents in both plots the declive of the strain vs stress curve which gives the Young Modulus (adapted from [34]).

Chapter 3

Designed Sensor Fabrication and Characterization systems

3.1 TMR Sensors Microfabrication - techniques and processes

The fabrication process of the TMR sensors took place in the INESC-MN facilities, namely in the class 10/100 clean room and the process was undertaken by Maria Carvalho and Rita Macedo. The microfabrication of MTJ elements comprises various steps to obtain the final, working result. The runsheet is annexed at the end of the document and those steps are indicated in the table 3.1. In this chapter they will be described in detail as well as the machines used in each of them.

The sensors were deposited on a Si substrate. Each die is composed of 16 sensors which in turn are made of 20 linearly aligned $20 \times 2\mu m^2$ MTJ elements.

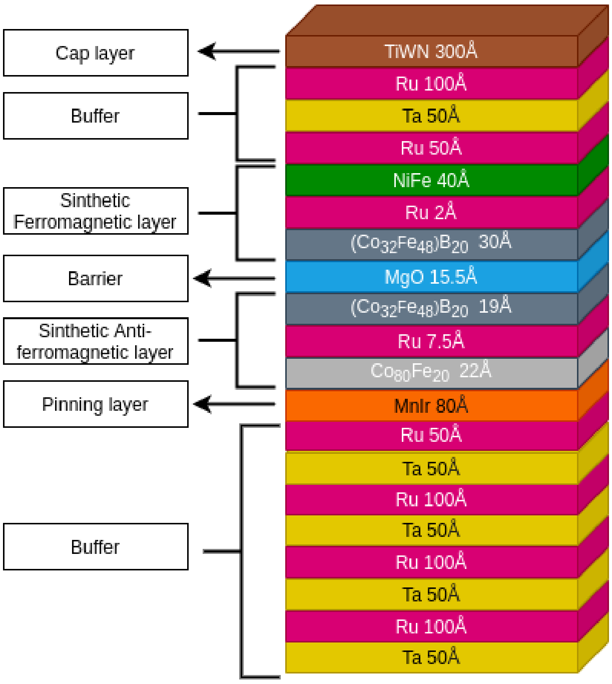

Figure 3.1: Schematic view of deposited stack.

The fabrication starts with the MTJ pillars definition. This begins with the deposition of the TMR stack and a *TiWn* cap layer in the combined N3600/N8800 system on Si substrate. The cap layer is needed as a sacrificial layer in the RIE process, while opening vias for the top pillar, to grant protection to the layers below.

In this step, the Ta, Ru, and TiWN layers are deposited in the N3600 module, by ion beam deposition (IBD) where as the $Co_{80}Fe_{20}$, $(Co_{32}Fe_{48})B_{20}$, MgO, NiFe and MnIr layers are deposited in the N8800 module by magnetron sputtering. The TMR stack deposited is schematically shown in image 3.1.

Step #	Process	Equipment
1	TMR stack and cap layer deposition	N3600 / N3800
2	Lithography - Pillar definition	SVG / DWL
3	MTJ pillar etch	N3600
4	Resist ashing	SPTS
5	Lithography - Bottom electrode definition	SVG / DWL
6	Bottom electrode etch	N3600
7	Resist ashing	SPTS
8	Passivation - SiO_2 deposition	Oxford
9	Lithography - Vias definition	SVG / DWL
10	Vias opening by RIE	SPTS
11	Resist ashing	SPTS
12	Metallization	N3600 / N8800
13	Lithography - Top electrode definition	SVG / DWL
14	Metal etch	SPTS
15	Resist ashing	SPTS
16	Passivation - SiO_2 deposition	Oxford
17	Lithography - Vias definition	SVG / DWL
18	Vias opening by RIE	SPTS
19	Resist Ashing	SPTS
20	Annealing	annealing setup

Table 3.1: Fabrication steps - summary.

This is followed by a lithography using the SVG/DWL systems where the sample is coated with 1.5 μm of photoresist to protect the areas where material is not supposed to be removed from, in this case the areas that correspond to the top of the MTJ elements' pillars. The photoresist will prevent the layers bellow it from being etched. The pillars are then defined by ion beam milling, again in the N3600 module, and the remaining resist is removed by ashing in the SPTS system.

The second part of the fabrication process is the definition of the bottom electrodes, which begins with a lithography to define their area and then proceeds to remove the excess material by ion milling, ending with the resist ashing, much like in the first part.

Lateral passivation to electrically insulate the top and bottom electrodes is the next step, which starts with the deposition of a 3000Å layer of SiO_2 in the *Oxford* system. A third lithography is then performed on top of the passivation layer to open the vias to the top of the MTJ pillars, resulting in a sample completely covered in resist except in the vias surface areas. The sample is then entered in the SPTS system to open the vias by reactive ion etching and a resist ashing step is then performed to remove the remaining resist.

The passivation is followed by the definition of the top electrodes part of the fabrication, which commences with the sample in the N3600 module of the N3600/N8800 system for a soft etch to remove impurities, it is then taken to the N8800 module for the deposition of a 3000Å *AlSiCu* layer, before being returned to the N3600 chamber where a 150Å layer of *TiWn* is deposited. This is again succeeded by a lithography to define the area of the top electrodes and finally a metal etch and a resist ashing step are performed in the SPTS system.

The final part of the process is a final 3000Å passivation layer, which starts with the deposition of said layer (SiO_2) in the *Oxford* system. A lithography to define the area of the vias is then performed, followed by a vias opening step and posterior resist ashing in the SPTS system. The fabrication process is also schematically summarized in Figure 3.2.

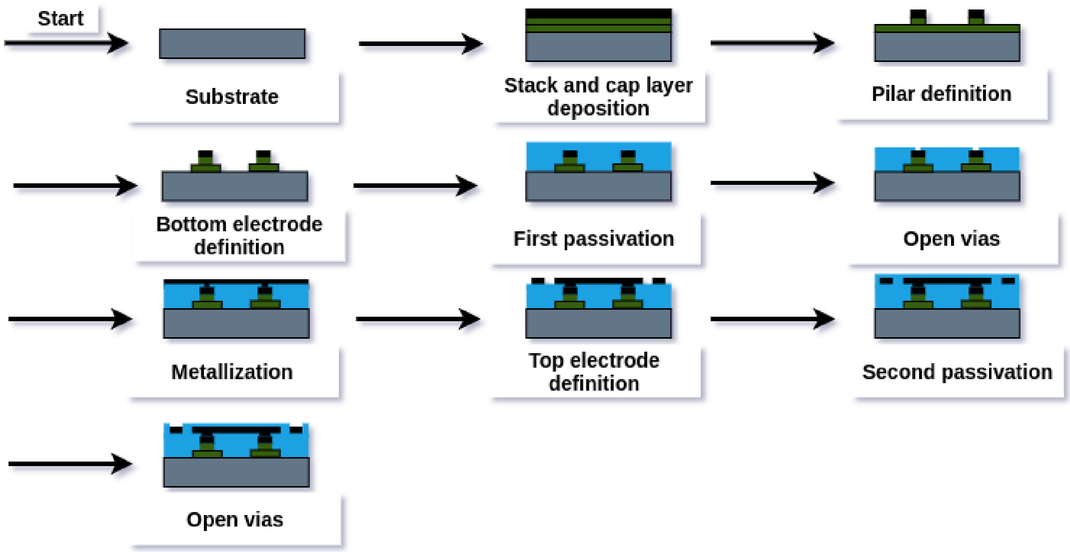

Figure 3.2: Summarized schematics of fabrication process of TMR sensors.

3.1.1 N3600/N8800

The Nordiko 3600/ Nordiko 8800 system is composed of two modules, the N3600 and the N8800, shown in Figure 3.3. These modules are connected to the dealer chamber that contains a robotic arm that handles the sample inside the, machine taking it where it needs to be in accordance to the process at hand. The dealer chamber is in turn connected to the loadlock chamber which serves as the entrance for the sample and, by being separated from the rest of the system, prevents the need for venting and pumping each time a sample is loaded.

Besides the ability to transfer samples from one module to the other during the same process, the N3600 module has 6 target slots and the N8800 has 8, which further increases the capacity of the system to accomplish the deposition of several different materials in the same process by switching to different targets.

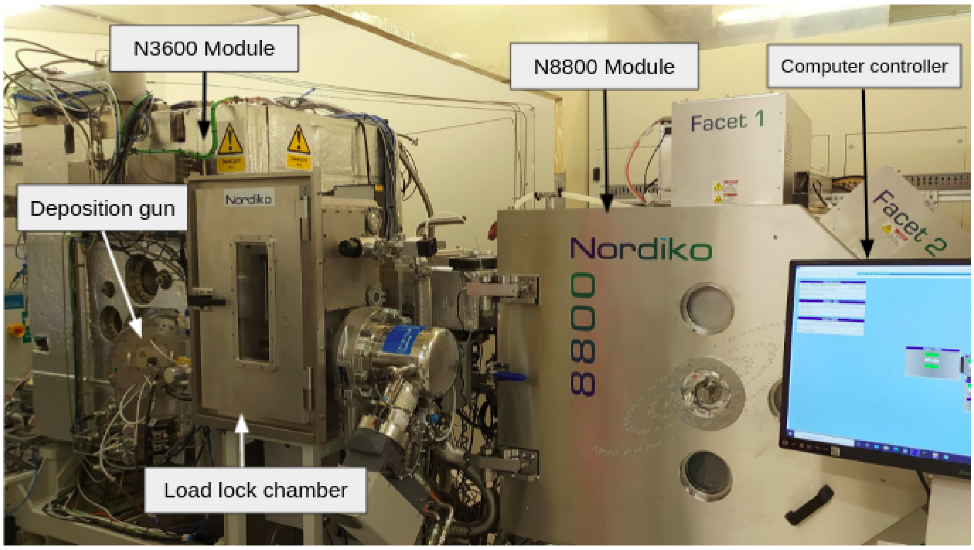

Figure 3.3: The N3600/N8800 system.

Ion beam deposition

Ion beam deposition [35] is a physical deposition process in which atoms from the desired material are removed from a target by transfer of kinetic energy from the ion beam. The Nordiko 3600, available at the INESC-MN facilities, can be used as an IBD system.

It works by creating a Xe plasma in a vacuum chamber in the deposition gun and accelerating and directing it towards the target with the help of a voltage difference applied to 3 grids which also serve as a collimator for the beam. The atoms ejected then hit the target of the desired material and the transfer of kinetic energy from the beam removes the atoms from the target (Figure 3.4). These will then get deposited in the surface of the sample, which will be at a specific angle so as to achieve the best rate of deposition possible. The sample will also be rotating at about 30 rpm to ensure uniformity in the process.

The Nordiko 3600's main chamber, where the deposition happens, is maintained in a ultra high vacuum (10^{-8} torr), this is achieved by gradually activating one of 3 pumps at a time - a rotary one, then a turbomolecular and finally a cryogenic pump.

Magnetron sputering

The layers deposited in the N8800 module are grown by magnetron sputtering [36], which is a physical vapour deposition method.

In a chamber subject to ultra-high vacuum, a plasma is created by the interaction of atoms of an inert gas that collide with free electrons trapped by a magnetic field created by a permanent magnet placed behind the target. These collisions release an electron from the gas atom, turning it into a positive ion. The ions will in turn be attracted and accelerated towards the target, which will be under a very high negative voltage. Once they hit the surface of the target, atoms will be ejected by transfer of kinetic energy, and since they are neutral they will not interact with the magnetic field or the negatively charged target, making it possible for them to travel across the vacuum and be deposited on the substrate.

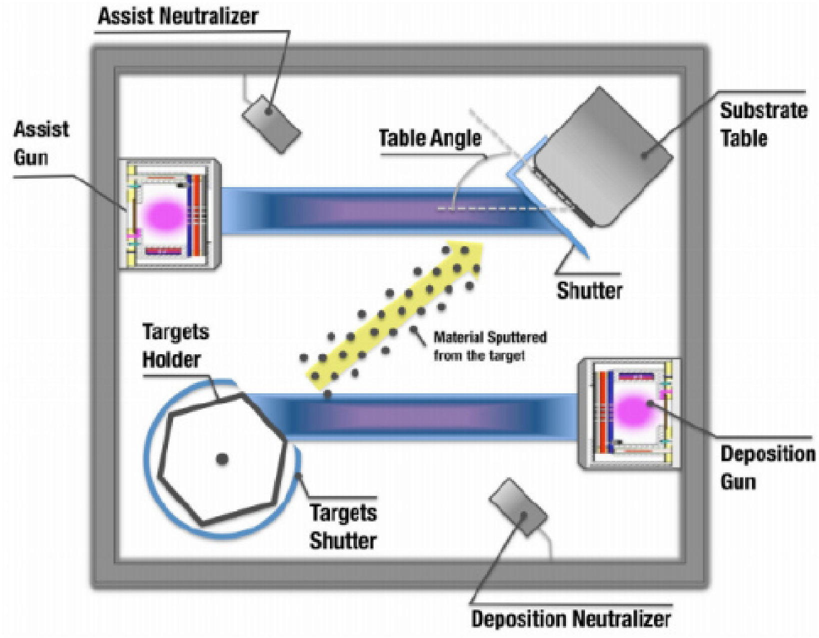

Figure 3.4: Ion beam deposition scheme [30].

Ion Beam Milling

In order to define the dimensions of the MTJ pillars or the bottom electrodes, the sample is put through a physical etching process to remove material excess - Ion Beam Milling. This happens again in the Nordiko 3600 module, where an Ar+ plasma is created in the assist gun. The ions are then ejected and directed towards the sample aided by the 3 voltage biased grids, when they hit the sample they remove material by sputtering.

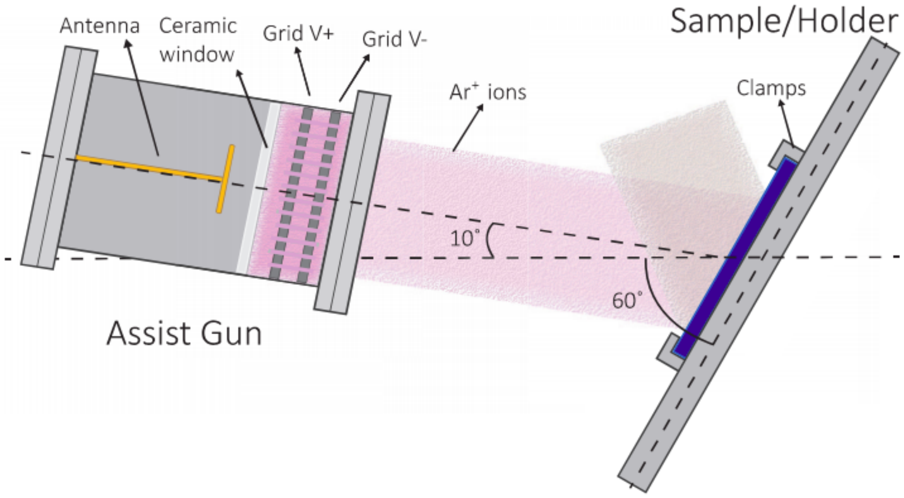

Figure 3.5: Ion beam milling scheme [37].

Physical etching is a non-selective method, which means it will etch any material the ions hit. Hence why it is important to do a lithography step to protect the top of the pillars against the plasma ions, preventing etching in undesired areas.

The sample angle will be alternated between 60º and 30º in the MTJ pillar definition and will be 45º in the bottom electrode definition to prevent re-deposition of etched material and the creation of trenches and it will be rotating at around 30 rpm to improve uniformity. The read values for the assist gun are presented in table 3.2 and a scheme of this process is shown in Figure 3.5.

		Power(W)	V+ (V)	I+ (mA)	V- (V)	I- (mA)	Ar flux (sccm)	Pressure (Torr)
Step 3	60º	180	657	104	348	3	15.9	1.25 $\times 10^{-4}$
	30º	189	656	104	348	4	15.9	1.24 $\times 10^{-4}$
Step 6	45º	180	656	104	348	4	16	1.23 $\times 10^{-4}$

Table 3.2: Read values of assist gun parameters for both etching steps.

3.1.2 SVG/DWL - Optical Lithography

Optical lithography is used whenever the fabrication process entails the deposition and posterior etching of material. In the end of this process one is left with a sample which is covered in resist in the areas which are intended to be protected from etching. The systems used here are represented in Figure 3.11.

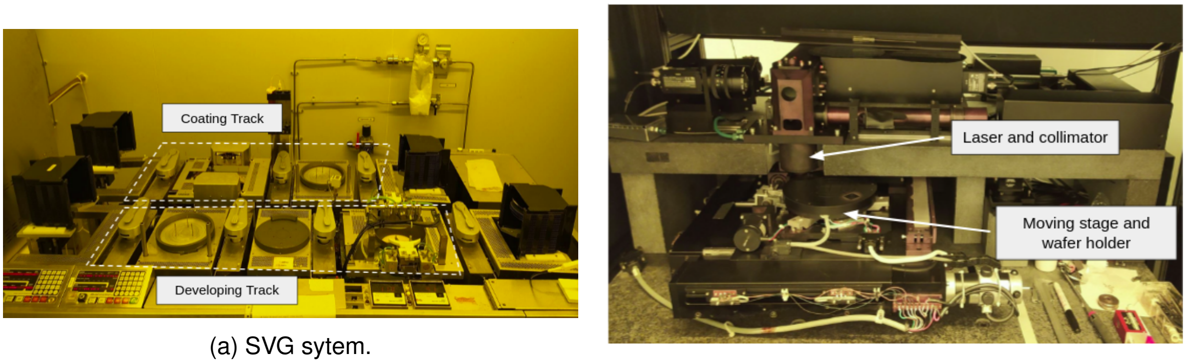

(a) SVG sytem.

(b) Heidelberg DWL 2.0 system.

Figure 3.6: Systems used in the optical lithography process.

This process starts with a pre-baking of the sample to 130 ºC in a vapor prime oven, to evaporate any water molecules left on the surface, in the presence of HDMS (hexamethyldisilizane) to promote the adhesion of the resist to the sample.

Using the coating track of the SVG system, the wafer is spun while being coated with a positive photoresistive polymer. Photoresists can be classified as positive or negative. A positive photoresist sees its chemical structure change when exposed to radiation of a certain wavelength, causing it to dissolve more easily (with negative ones, the inverse happens and exposed areas of the resist get harder to dissolve). After coating, a 1 minute soft-bake at 95ºC follows, with the purpose of evaporating any solvents left.

It will then be exposed to laser light, by means of the Heidelberg DWL 2.0 system, which is composed of a motorized stage that moves the sample below a 400 nm diode laser. A software mask made with CAD software with the information about which areas to expose is created and converted to .lic files which can be read by the laser system's software as columns of 200 micrometers width, which will be exposed by the laser one at a time.

In the final stage of this process the sample is put on the development track of the SVG system, heated until it reaches 110ºC and then cooled down. The developer is then applied and once the development time is over, the sample is sprayed with deionized (DI) water to wash away the developed portions of the resist.

To prevent the incidence of radiation on the sample which might lead to the photoresist premature degradation, the lithography is undertaken in a room with windows that filter out light of the specific wavelengths that cause damage to the resist.

3.1.3 SPTS

The SPTS system is a machine that carries out reactive ion etching processes. It can etch SiO_2 as in steps 10 and 18, with the purpose of opening the vias for the pillars or the metal contacts. In steps 4, 7, 11, 15, 19 resist ashing is done also in this system, where all the resist remaining after the several etch steps is removed. And it is also utilized for etching metal in step 14 for defining the top electrode and the metallic contact pads.

This system includes a loadlock chamber where the sample enters the machine, a chamber where the RIE processes take place and a dealer chamber with a robotic arm that transfers the sample from the loadlock to the chamber and vice-versa.

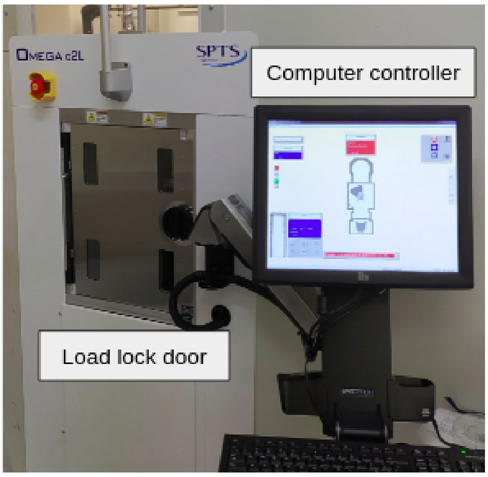

Figure 3.7: View of the SPTS system.

In a reactive ion etching process [38], an inert gas sitting between two parallel plates is excited into a plasma in low pressure conditions. This originates reactive ions that will be accelerated towards the substrate that is placed in a charged electrode. These same ions will also be selected to react with the material on the substrate, chemically etching it. Therefore this method can achieve high directional etching because of the perpendicular impact of the incoming ions and also high etching rate product of the chemical reactions between the samples' surface materials and the etching species.

3.1.4 Oxford PlasmaPro 100

The deposition of the passivation layers (SiO_2) is done in the Oxford PlasmaPro 100 system, the set-point values of the the conditions of these depositions are presented below in table 3.3. This machine consists of a loadlock chamber where the sample is entered into the system and a process chamber where the deposition is undertaken by plasma-enhanced chemical vapour deposition (PECVD) [39].

PECVD allows to deposit various thin films, among which SiO_2 is included. In this process electrical current is used to produce a glow discharge in the gaseous mixture. The energy from this discharge excites the components of the gas mixture into a plasma. These components are then directly deposited onto the substrate through interaction with it.

The energy of the electrical current applied is sufficient to sustain collisions between electrons and molecules in the plasma that create reactive species, allowing for the deposition to be made at lower substrate temperatures, which is the main advantage of PECVD.

Figure 3.8: Oxford system for deposition of passivation layer.

	Gas Flow (sccm)				
Total time	N_2O	SiH_4	N_2	Temperature (ºC)	Power (W)
3 min 50 s	710	8.5	161.5	300	20

Table 3.3: Set-point conditions for the deposition of the passivation layers.

3.1.5 Annealing

After fabrication, it is necessary to define the direction of the pinned layer magnetization through annealing. This is done in the annealing setup at the INESC-MN facilities. In this system the sample is heated in a furnace until it reaches a certain temperature and then left to cool down until room temperature in the presence of a strong constant magnetic field. For this particular process, the sample was annealed for 2 hours in the presence of a 1T magnetic field at 330ºC generated by a Hallbach array [40].

3.2 Auxiliary fabrication methods

After the microfabrication of the TMR sensors, one has prepare them to be able to acquire the output data. The elastomer pieces which are part of the designed sensor also have to be fabricated. These processes are described in this section.

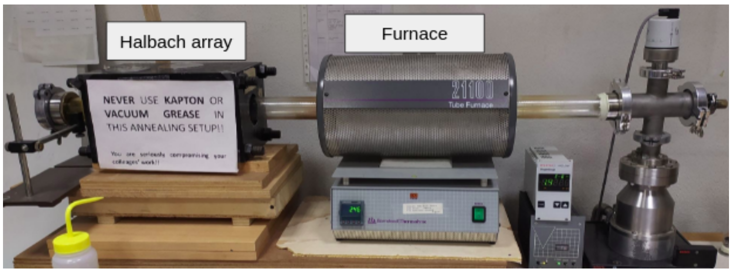

Figure 3.9: Annealing setup.

3.2.1 Die Dicing

After fabrication, the sample is still constituted by several sensors dies. Therefore, in order to be able to manipulate and use them individually, one has to separate them.

This process is called dicing, in which the sample is sawed in the spaces between the sensor dies in the Disco DAD 321 automatic dicing system which is presented in the Figure 3.10.

Figure 3.10: Dicing machine.

The sample is covered with a layer of resist beforehand, to help protect against particles of sawed material (and when in operation the dicing system streams a jet of water over the sample to stop flying particles). Then it is held in place with a photosensitive adhesive tape in a metallic frame that fits into the dicing system.

After placing the sample in the machine, one has to align it and define the parameters of the operation such as cutting speed. A saw of 150 μm thickness was used in this process.

The final step in this process, after the sample is diced, is to place the metallic frame with the sample under UV light for a few minutes in order to weaken its adhesion.

3.2.2 Wirebonding

After securing the sensor dye in the chip carrier it is necessary to connect the pads in the sensor die to the ones in the chip carrier. This is done in the K&S 4526 Manual Bonding system (shown in picture 3.11a) which uses aluminum wire for this purpose.

The connections are then covered with a layer of black epoxy to protect them against mechanical damage and in this case, also to shield against light.

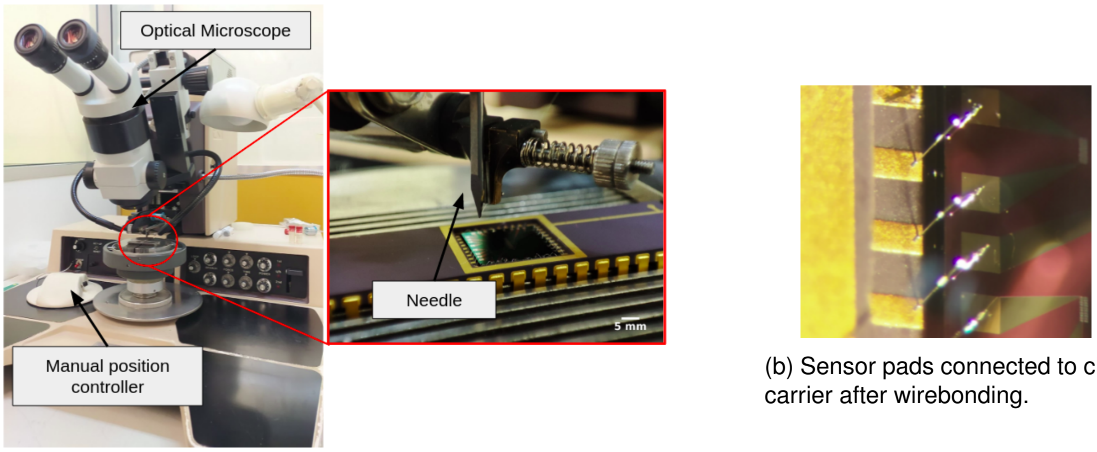

(a) Wirebonding system.

(b) Sensor pads connected to chip carrier after wirebonding.

Figure 3.11: System used in the wirebonding process and result.

3.2.3 Fabrication of EcoFlex parts

The soft parts of the sensor were made of the commercial silicon based elastomer *Ecoflex*^{TM} 00-30 [41]. This material is cheap, easy to manipulate and use and highly elastic.

For the fabrication of the *EcoFlex* parts, molds were designed in the software *FreeCad* and 3D printed. In Figure 3.13 the molds used and the resulting *EcoFlex* pieces are shown, 4 different were produced with the goal of testing different magnetization distributions. From left to right in the picture: for 1 permanent magnet, for 5 permanent magnets, for homogeneously distributed magnetic particles and for magnetic particle ”islands” (CAD drawings for all of the configurations are shown in Figure 3.12).

EcoFlex comes in 2 parts, one in each of 2 containers, that harden when mixed in a 50:50 mass ratio. So, using a precision balance, both part A and part B are added to a container in equal quantities and then mixed. For the case of homogeneously distributed magnetic particles, those were also added to the same container with the *EcoFlex* in a 40:60 (*EcoFlex*:Magnetic Particles) mass ratio. The magnetic particles used are NdFeB particles of $\sim 5\mu m$ diameter (MQFP-B+-10215-089, Molycorp Magnequench).

The mix is then placed for around 15 minutes in a Vacuum Desiccator in order to remove the air bubbles formed during the mixing process. Finally, aided by a syringe, the mix is injected into the mold and left to harden for 4 hours at room temperature. After removing the *Ecoflex* from the molds, the magnets were placed in their position. In the case of the piece with the magnetic particle ”islands” a mix of *EcoFlex* and Magnetic Particles at a 40:60 mass ratio is injected into the holes in the piece after it

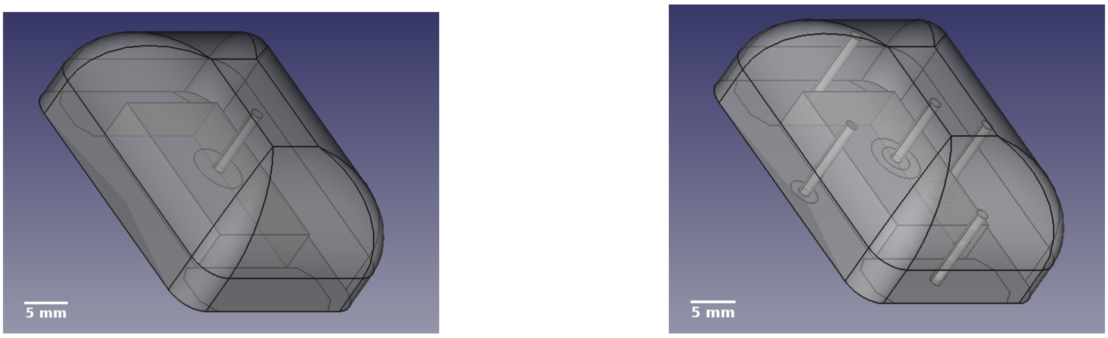

(a) *EcoFlex* piece with 1 permanent magnet, the magnet is inserted from the bottom of the piece until the top of the cylinder hole.

(b) *EcoFlex* piece with 5 permanent magnets, the magnets are inserted from the bottom of the piece until the top of the 5 cylinders holes.

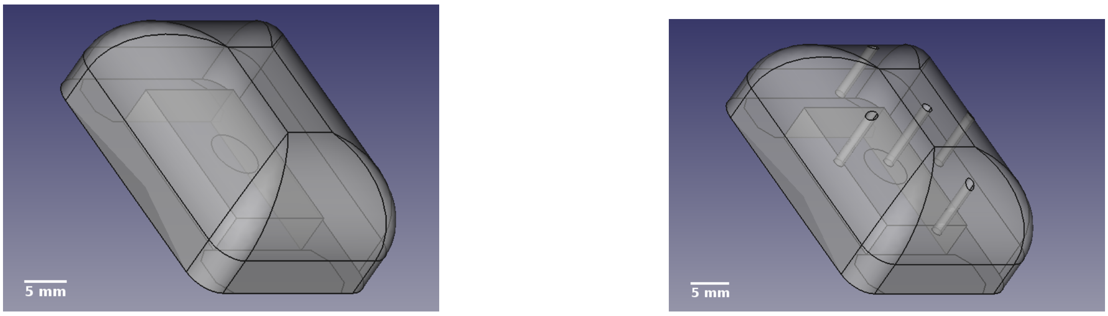

(c) *EcoFlex* piece homogeneously magnetized with magnetic particles at a 40:60 (elastomer:magnetic particles) mass ratio.

(d) *EcoFlex* piece with 5 magnetic particle ”islands”, the mixture of *EcoFlex* and Magnetic Particles at a 40:60 mass ratio is injected into the cylinder holes.

Figure 3.12: CAD drawings for the 4 *EcoFlex* pieces used in this work.

cured.

In the case of the magnets these were embedded in the elastomer piece to align the direction of their magnetic moment with the sensitive direction of the TMR sensors. The magnets used were NdFeB, N45 grade magnets of 2 mm height and diameter. The pieces with magnetized *EcoFlex*, be it the one with homogeneously distributed particles or the one with magnetized elastomer islands, they were annealed for 1 hour and a half at 135ºC in the presence of a 1T magnetic field in such a way as to also align their magnetic moment with the TMR sensors sensitive direction.

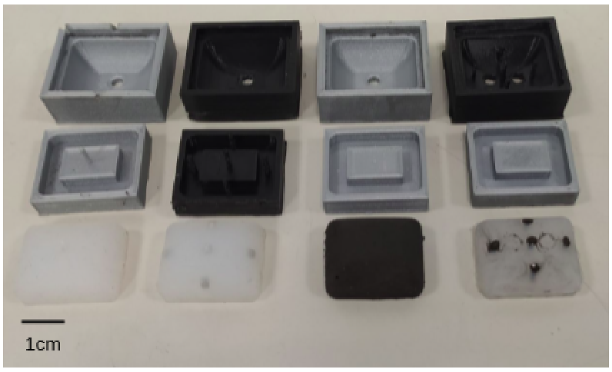

Figure 3.13: 3D printed molds and corresponding *EcoFlex* parts.

3.3 Characterization

3.3.1 Magnetotransport curve measurement

To characterize the magnetoresistance of the sensors, a setup is used that consists of a current source (Keithley 220), a voltmeter (Keithley 182), an optical microscope, a pair of Helmholtz coils and their current source and 4 micropositioner tungsten needle probes. This setup is shown in Figure 3.14.

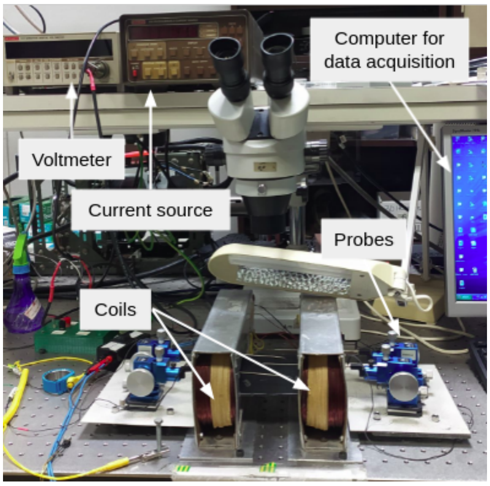

Figure 3.14: 140 Oe Setup.

The measurements made in the sensors used in this work only require the use of 2 probes. By positioning the probes in the pads of a sensor, a constant current is passed through it (in this case of $1\mu A$). Meanwhile a computer software is used to control the coils' current source, generating a constant magnetic field between them sweeping from -140 Oe to 140 Oe. For each step of the sweeping magnetic field, the software, which is also connected to the voltmeter, receives the output voltage of the sensor, calculates the resistance and generates the magnetotransport curve, which allows the visualization of the behaviour of the resistance in relation to the applied magnetic field. Besides these, the software also calculates important quantities such as the MR(%) and coercivity field.

3.3.2 Force test Setup

The reconstructed motorized precision movement stage (Chapter 4) is used in combination with the ATI Force and torque *Nano17* sensor [42] to test the magnetic sensors designed. The *Nano17* force sensor used the SI-50-0.5 calibration, which means it had a force resolution of 1/80 N. The force test setup was composed of the magnetic sensor and the magnetized *EcoFlex* piece, the data acquisition board (which was put in a 3D printed piece that helped holding it steady and stopped it from interacting with the metal parts of the stage), and the force sensor, which was attached to the Z axis of the stage and made to apply a force on the *EcoFlex* by its movement. The force sensor data was acquired by a National Instruments acquisition module (NI DAQPad-6251) . An image of the setup is shown below (Figure 3.15).

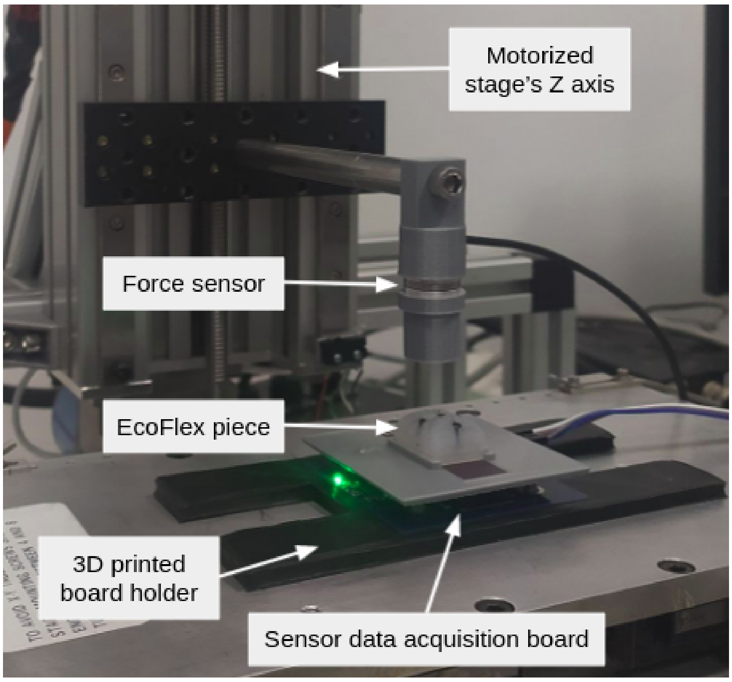

Figure 3.15: Setup for experimental data acquisition.

Using this setup, for each of the *EcoFlex* pieces several experiments were performed which are detailed in Chapter 6.

It is important to note that since the force sensor has components that interact magnetically, besides reducing the force application area, the indenter serves the purpose of creating a separation between the force sensor and the *EcoFlex* piece large enough for the magnetic field created in them to not suffer interference by the force sensor.

3.4 Uniaxial traction tests

In order to characterize the mechanical properties of the *EcoFlex* parts, an uniaxial traction test was performed on test samples for both pure and magnetized *EcoFlex*. The tensile specimen were fabricated through molding. A mold was made using two acrylic plates. One of them was machined in a CNC system with the shape of the specimen using the respective G-code file. It was then attached to the other one through acetone welding. Finally the mold and another acrylic plate used as a cover were drilled in several places to allow for the insertion of screws to hold the mold and cover to get the specimen with the desired dimensions. The test samples and mold are presented in Figure 3.16.

The traction tests are performed in a mechanical test frame, in this case the *INSTRON 5966* system is used (Figure 3.17). The tensile specimens are held by the test frames' grips (as pictured below) in such a way as to align them correctly (by the top and bottom lines shown in the specimens on Figure 3.16) and also grip them tight enough to avoid slipping. After placing the sample in the grips, these are moved manually until the specimen is stretched but the stress applied on them by the test frame is null. The traction test itself consists in applying stress monotonically to failure at a single strain rate (in this

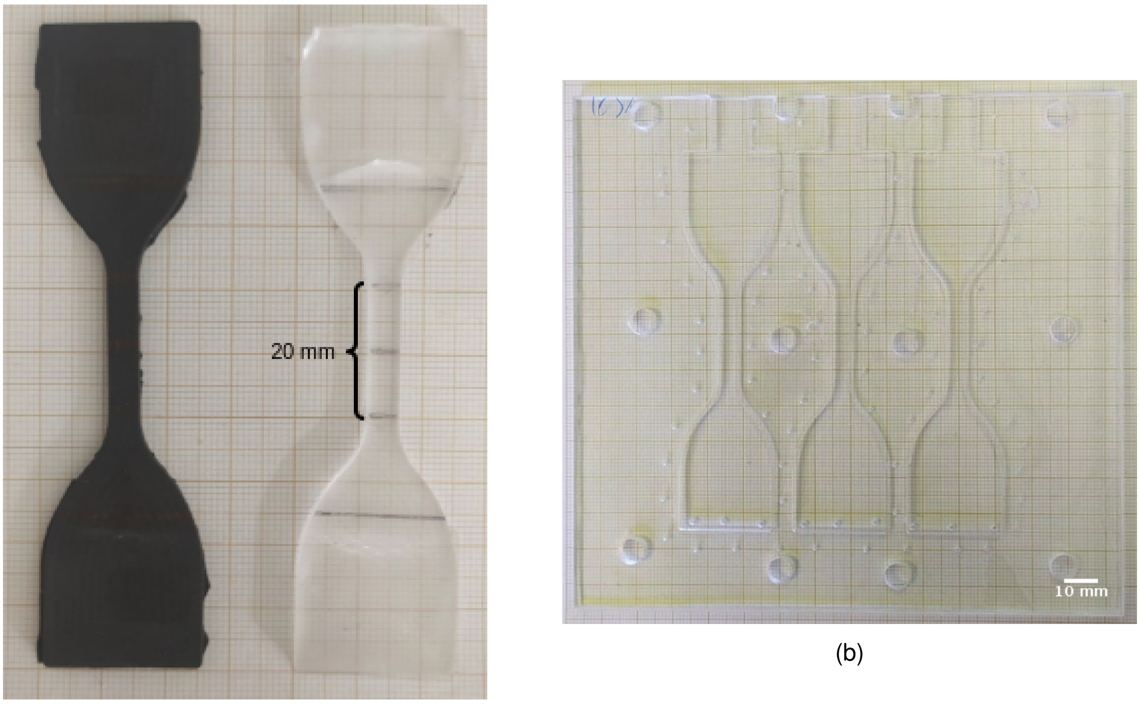

(b)

(a)

Figure 3.16: *EcoFlex* test samples for uniaxial traction testing: piece magnetized with magnetic particles in a 40:60 (*EcoFlex*:MPs) ratio (left) and pure *EcoFlex* piece (left). Tensile specimen mold (right).

case of 500 mm/min) by means of a movement actuator that displaces the upper grip in the upwards direction. A computer records the load applied on the sample and also the strain, the latter is computed as the displacement of the 20 mm portion of the specimen shown in Figure 3.16.

The uniaxial tests performed in this work as well as the values calculated posteriorly were done in compliance with the ISO 37:2017 Standard, which specifies a method for the determination of the tensile stress-strain properties of vulcanized and thermoplastic rubbers.

After the calculations are made, a Strain vs Stress plot is obtained which is analyzed to obtain model parameters. It is important to note that it is considered that the cross-section of the specimen is maintained constant throughout the test and that only the 20 mm portion referred earlier suffers significant strain.

3.5 SQUID magnetization measurements

In order to obtain information about the magnetic properties of magnetized *Ecoflex*, to use in the magnetic simulations in Section 5.3, SQUID (superconducting quantum interference device) measurements were made on 60:40 mass ratio (*EcoFlex*:MPs) magnetized elastomer.

SQUID is a device that consists of a superconducting loop interrupted by thin insulating layers called Josephson junctions through which current flows by magnetic tunneling. The SQUID allows a bias current to divide into 2 paths of the loop, because of the existence of the Josephson junctions the voltage over the loop will be a function of the magnetic flux through the loop. The voltage is amplified and the

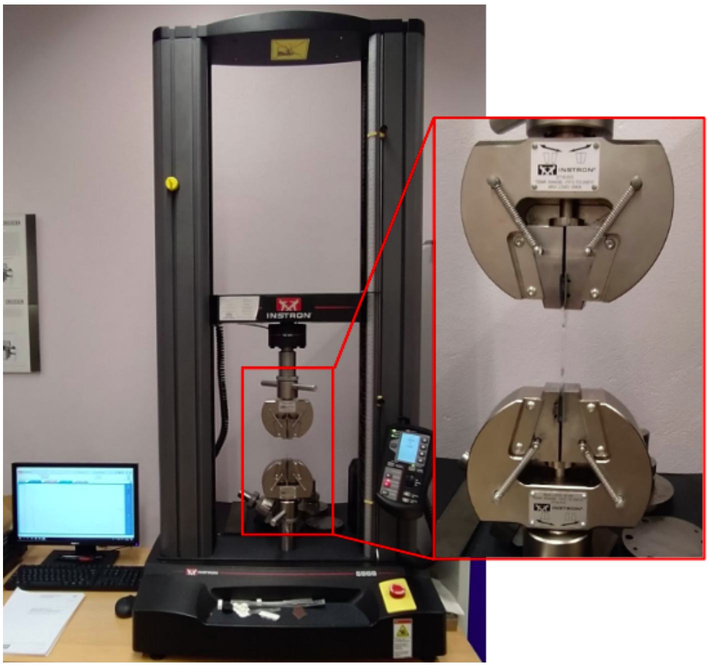

Figure 3.17: *INSTRON 5966* mechanical test frame and closeup of grippers.

magnetic field strength can be determined [43]. By inductively coupling the SQUID to a superconducting detection loop (magnet) it is possible to detect variations in magnetic flux in this loop by the insertion of a sample. Information about the magnetic properties of this sample can be obtained by changing the applied magnetic field (hysteresis loop). The SQUID system used in this work is shown in Figure 5.5 as well as a schematic of the working principle of detection.

In this thesis, the measurements were made in the SQUID magnetometer system of the Campus Tecnológico e Nuclear of the Instituto Superior Técnico. The magnetized elastomer samples were prepared beforehand and taken to measure. After inserting the sample in the superconductive loop, the external magnetic field is swept from 5×10^5 Oe to -5×10^5 Oe and back again giving, as the final product, the hysteresis loop of the sample, which is then ready to analyze. It is noted that the measurements were taken at a temperature of 290K.

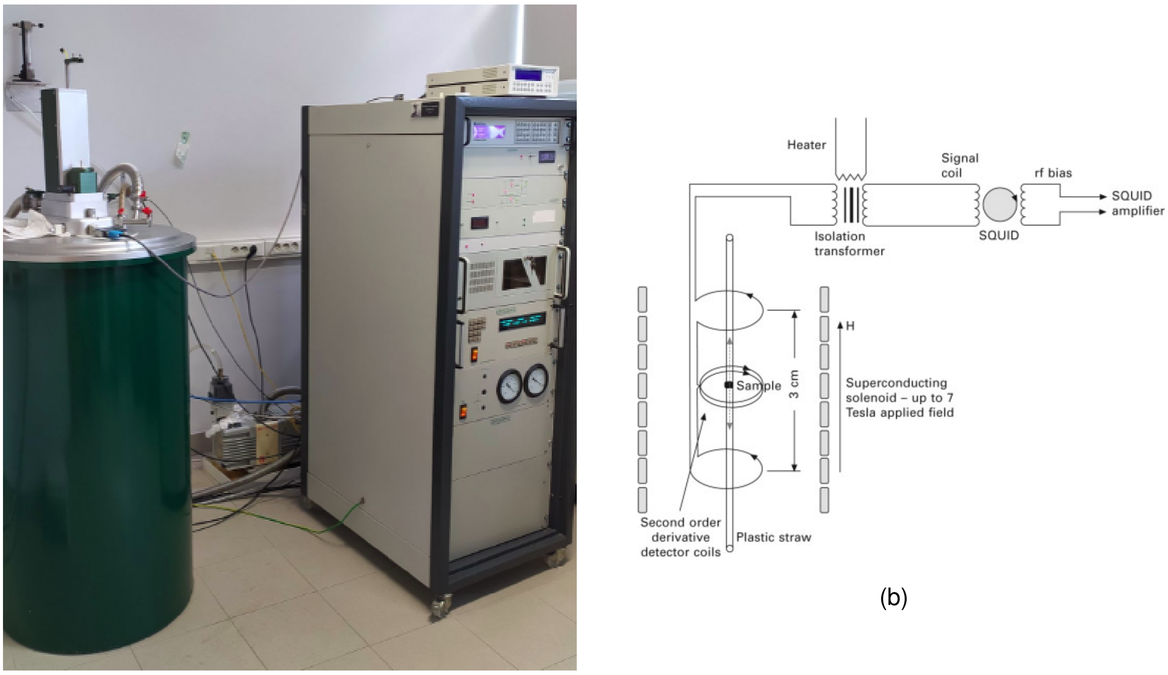

(a)

(b)

Figure 3.18: *CRYOGENIC Ltd* S700X SQUID Magnetometer used in this work. It is located in the Campus Tecnológico e Nuclear of Insituto Superior Técnico (left). A schematics of the working principle of a SQUID magnetometer such as the one used. The sample is inserted in the superconductive magnetic loop inside a straw, the magnetic field variation is then sensed by the SQUID loop [44].

Chapter 4

Repurposing of 3D precision movement stage

A necessity arose of a setup where the tactile sensors could be tested. As a part of this setup, an apparatus capable of precision movement was needed and therefore an old precision movement stage originally used for wirebonding was repurposed and restored for that goal. This part of this thesis was done in collaboration with Rita Pagaimo and Pedro Ribeiro.

The reconstruction process is described in the next chapter, including dimensioning, electrical connections and programming the movement.

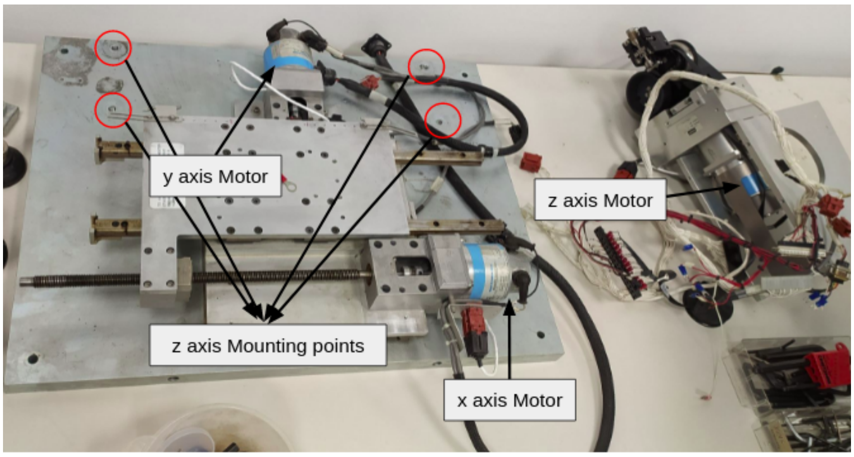

Figure 4.1: The precision movement stage before repurposing.

4.1 Dimensioning of Z axis

Since the stage had been unused for some time, the first step was to test the encoders of the electrical stepper motors with an oscilloscope to see if they worked. After supplying them with current and verifying that it was translated into the movement of the rotary shaft of the motors, the stage was disassembled, its parts cleaned and then assembled in their place again.

The stage's x and y axes were complete, but the z axis was missing, although a motor identical to the one used in the other 2 axes was available - as can be seen in Figure 4.1. So, knowing that the motors were working, the dimensioning and design of z the axis frame and motor socket were the next priority.

Several design considerations were made in the process of designing and assembling the z axis,namely:

- it would be constructed on the same side of the metal table as the y axis, because of the space available and the previous existence of holes that allow mounting the axis frame;
- The axis would be elevated, firstly due to the requirement that it is leveled with the x and y axes moving plate, and secondly because of the bottom placement of the y axis motor;
- The motor would be placed on top of the axis frame, so as to connect directly to the rolled ball screw shaft that would provide the dislocation of the axis movement plate;

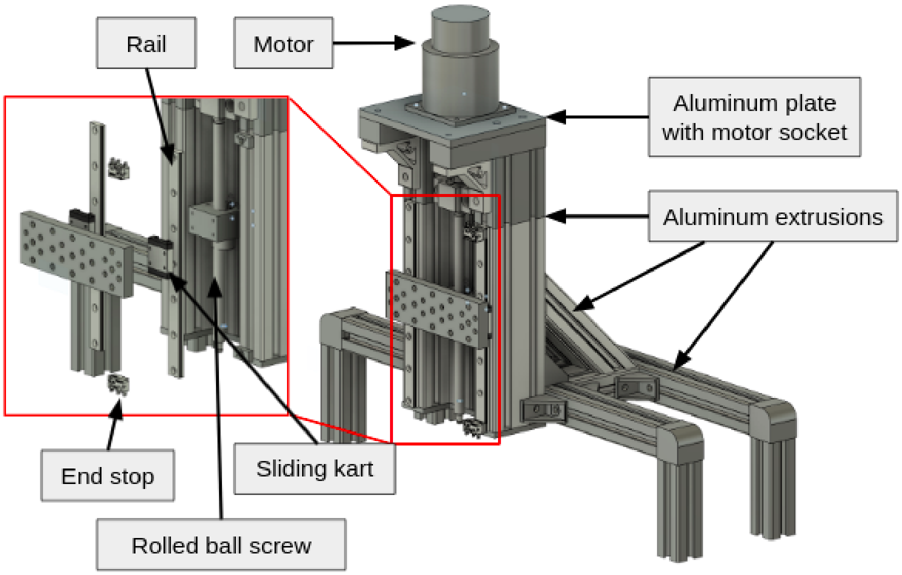

Figure 4.2: Z axis schematics: view and parts.

The pieces needed for this process were bought in the online hardware store *MiSUMi*. *MiSUMi* provides the CAD drawing file of every piece available for purchase. After taking the dimensions needed and planning the design of the stage, these CAD drawings were imported and put together in the desired manner in the *Autodesk Fusion 360* software for a first overview of the assembled axis. This made it easier to make the needed adjustments and check for errors in the design. In figure 4.2 is an image taken from the *Autodesk Fusion 360* software of the z axis. This is a schematics of the axis posteriorly built. In a general manner, the components used in the construction of the z axis were;

- Stepper motor;
- Rolled ball screw that transmits the movement from the motor to the axis moving plate;

- Roller linear rails: the plate is screwed to a kart in each of the rails allowing it to slide up and down without any other degree of freedom;
- Endstop switches: in the top and bottom of the desired moving range. When acted upon, they emit an electrical signal, allowing to stop the movement of the plate;
- Aluminum plates and extrusions used to form the structure of the axis and hold all the other components in their designated place;

4.2 Stage's electrical connections and components

To be able to program the stage's movement, it was first needed to connect the 3 motors and EndStop switches to the computer in a way the output data could be analyzed. The general connections between components are summarized in Figure 4.3 (for a more detailed electrical connections' scheme please refer to Appendix C.)

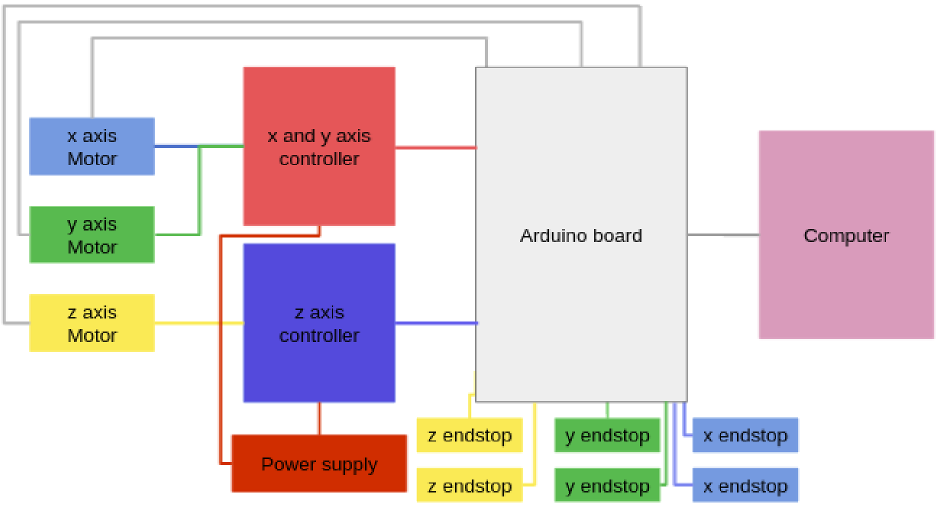

Figure 4.3: Electrical connections diagram.

The energy needed for the motors to function is supplied by the power supply, through the controllers. These can control the performance of the motors and parameters such as speed, direction of rotation and others by receiving information from the *Arduino* board and using it to control the current supplied to them. The motors' encoders can sense movement in either direction by counting "steps" since the beginning of motion and they supply information related to the motor steps to the *Arduino* board which are key to define the velocity and positioning of the motor. This board is then responsible for the PWM (pulse width modulation) of the motors, effectively controlling them by modulating the current supplied through the controllers, thus completing the cycle. In this work, an *Arduino Mega 2560* was used.

Besides this, the EndStop switches also provide the *Arduino* board with a signal that allows it to know if they have been actuated on (if the plate reached the limit of movement).

The *Arduino* board basically does the integration of all the electrical signals at play. It is then connected to a computer where the user can work with these signals and use them to program the movement of the motors and hence the stage, as described in the next section.

An image of the precision movement stage after repurposing and electrical connections are done is shown below.

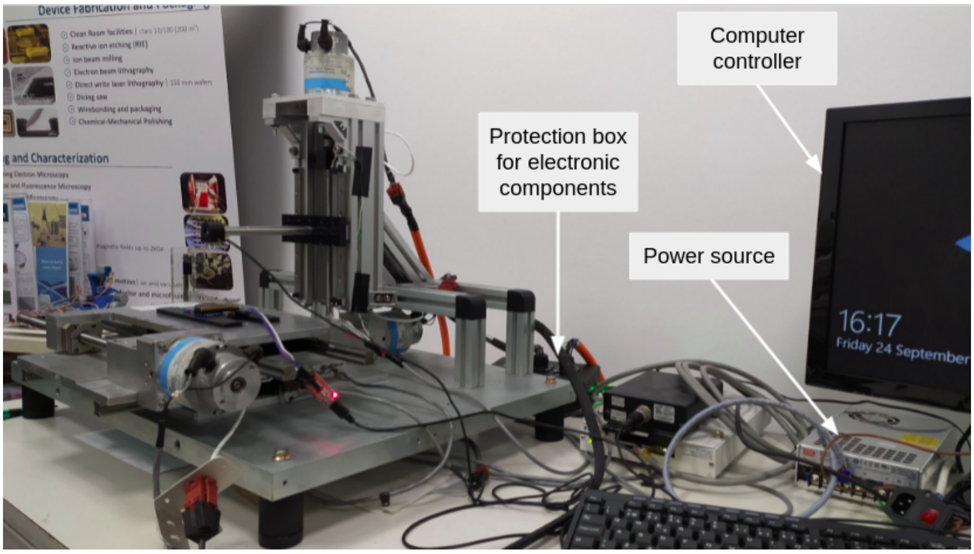

Figure 4.4: Completed stage (after repurposing).

4.3 Programming

The programming of the precision movement stage was done on the *Arduino IDE* in C++ programming language. The first step was to import an external ”Encoder” library that allowed to read the motors' encoder signals and turn them into motor steps by counting quadrature pulses from the encoders. This made possible the positioning and velocity control of the motor in an efficient way, by knowing the the ”step” the encoder was in at any given time.

Other than this imported external library, everything was programmed from scratch. A library was created where one can create an *axis* object, that has fro inputs the pins of the *Arduino* board that correspond to the motor encoders, the PWM for motor velocity and frequency modulation control and the EndStop switches. A velocity function was created that takes an int as input and writes that number into the PWM pin, that number will be translated into speed of the motor: the higher the number, the higher the speed. If the number is negative, the motor moves in the opposite direction. A *GetPosition* function was also devised, by reading the values of the encoder pins and outputing their value in steps. These two functions allowed for the creation of a third one that is used to move the plate by the input distance in μm. These function is called *GoToPosition* and works by making the motor move in the direction wanted and stopping when the difference between the current position and the initial one is zero. With these functions, one can perform the necessary tasks to test the sensors.

Additionally to this, two more functions were created, one to check the state of the EndStops switches and another one to Home the stage, that moved both the x and y movement plate and the z movement plate to the extremes of their movement range to know the range lenght in steps, and then ordering the plates to go to the middle of it. The Home function allows to know the exact location of the plates by resetting the values of the encoders to zero when they reach the firs limit of the range of movement. (The *Arduino* code is presented in the Appendix B).

Chapter 5

Simulations

A simulation of the device developed in this thesis was performed, with its description being made in this chapter, including simulation models and software parameters. The simulations were made using a finite element method (FEM) with the *COMSOL Multiphysics 5.5* software. FEM is a numerical method in which partial differential equations are solved. The system under study is is divided into smaller, simpler elements of user defined size and shape and then these elements are reconnected resulting in a set of linear equations that are more easily solved by the software.

This simulation is divided into two parts. The first part consists in simulating the deformation of the *EcoFlex* pieces for applied forces. This will be made for the pure *EcoFlex* pieces and also the pieces magnetized with embedded magnetic particles, which have different mechanical properties. Since no satisfactory reports of the mechanical properties of the elastomer use in this work existed in the literature, a uniaxial traction test was also performed (described in Section 3.4) in both normal and magnetized *EcoFlex*. The data was then fitted to obtain linear and hyperelastic model parameters that are used in the simulations, these results are also presented in this chapter.

The second part of the simulation consists in importing the deformed mesh from the first part and simulating the magnetic field in the TMR sensors position. Joining both results it is possible to know the magnetic field in the sensors' positions as a function of the force applied.

Since the variables of the systems are designed to coincide with the real life system when it comes to geometry, materials, permanent magnets and TMR sensors positioning and dimensions, it will be possible to compare the experimental with the simulated results. Also the indenters used to apply the forces to the system are mimicked in terms of shape in the simulations for a more accurate result.

5.1 Uniaxial traction test results

Since the mechanical properties and consequently the hyperelastic model parameters change significantly depending on the preparation and conditions of cure, in order to obtain the Young's Modulus and the hyperelastic model parameters needed for the simulations, an uniaxial traction test was performed on both materials (as reported in section 3.4). The resulting stress vs strain data was fitted to several models in order to obtain the parameters needed. The fits are made assuming isotropy and incompressibility of the material and the results are fitted to the the first Piola-Kirchhoff stress expressions for uniaxial deformation. These expressions are as follows (for more information refer to [45]):

- Neo-Hookean model: $P_1 = \mu(\lambda - \lambda^{-2})$
- Mooney-Rivlin of 2 parameters: $P_1 = 2(1 - \lambda^{-3})(\lambda C_{10} + C_{01})$
- Mooney-Rivlin of 5 parameters: $P_1 = 2(1 - \lambda^{-3})(\lambda C_{10} + 2C_{20}\lambda(\lambda^2 + \frac{2}{\lambda} - 3) + C_{11}\lambda(2\lambda + \frac{1}{\lambda^2} - 3) + C_{01} + 2C_{02}(2\lambda + \frac{1}{\lambda^2} - 3) + C_{11}(\lambda^2 + \frac{2}{\lambda} - 3))$

where λ is the strain and μ, C_{10}, C_{01}, C_{20}, C_{02} and C_{11} are the parameters to obtain.

5.1.1 Magnetized *EcoFlex* tensile specimens

The results and fitted expressions for the uniaxial tests performed on the magnetized pieces are presented in Figure 5.1 for the 3 tensile specimens which resulted in valid uniaxial tests. It is noticeable that all the expressions fitted agree with the results quite well, with values of R^2 bigger than 97% for each of the fitted models. Due to poorly fitting the data, the fit relating to the linear model is not shown in Figure 5.1. The 2 parameter Mooney-Rivlin model and the Neo-Hookean model are not adequate to model the behaviour of materials under large deformations: this explains the poor fit obtained when trying to fit the experimental data with these models in the whole domain. With this under consideration, they were used to fit only small strains, in the order of 2/2.5 times.

The results of only one sample test are shown because the experimental results are consistent among the 3 specimens, which behave the same way throughout the strain domain. The breaking point is quite different for each of them, with the plot shown in Figure 5.1 referring to the specimen that withstood the largest strain, this discrepancy can be justified by intrinsic properties of each sample such as air pockets or magnetic particle aggregation.

The average parameters obtained from the fitted expressions were the following:

- Neo-Hookean: $\mu = 42315.49\ N/m^2$
- 2 parameter Mooney-Rivlin: $C_{10} = 32017.66$ Pa; $C_{01} = -20336.20$ Pa;
- 5 parameter Mooney-Rivlin: $C_{10} = -60575.00$ Pa; $C_{01} = 92823.04$ Pa; $C_{20} = -12.12$ Pa; $C_{02} = 28818.60$ Pa; $C_{11} = -450.97$ Pa;

5.1.2 Pure *EcoFlex* tensile specimens

The results and fitted expressions for the uniaxial tests performed on the pure *EcoFlex* pieces are presented in Figure 5.2 where R^2_{MR} refers to the values of the R^2 parameter when fitting data with the 2 parameter Mooney-Rivlin mode, and R^2_{NH} when fitting with the Neo-Hookean model. It is important to mention that the values of strain vs stress for both the specimens considered were not consistent for

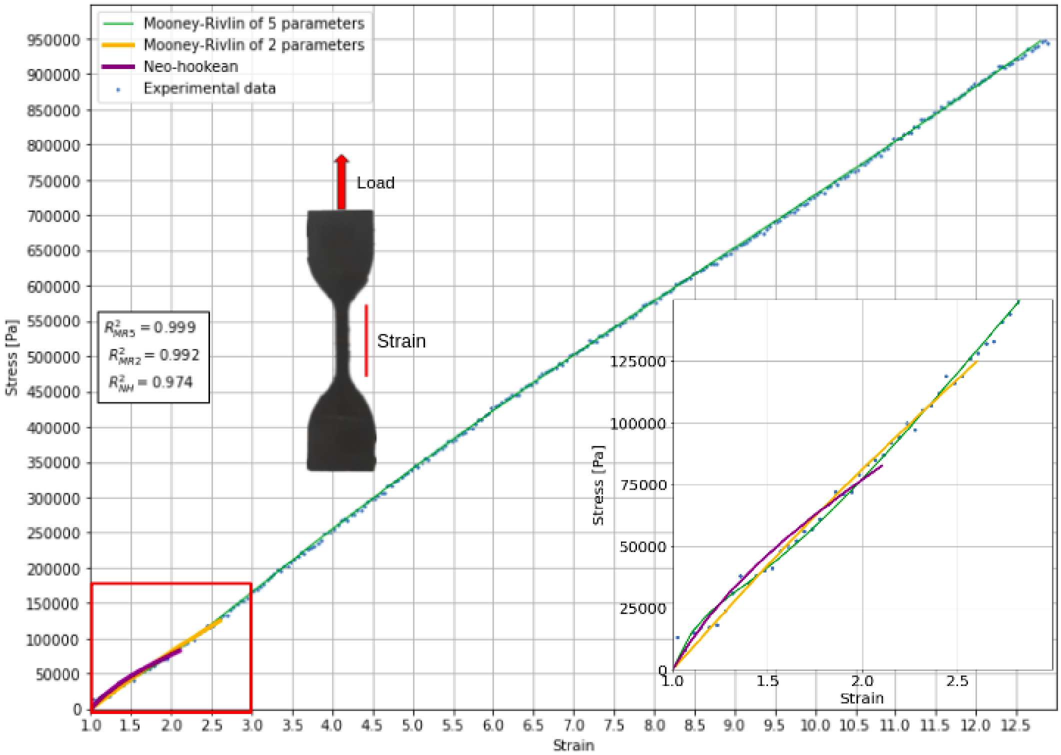

Figure 5.1: Experimental uniaxial traction test results and fitted models for one tensile specimen of magnetized *EcoFlex*.

higher values of strain. Therefore it was decided to consider only small deformations (up until 4 times) and for that reason, the results were not fitted with the 5 parameter Mooney-Rivlin model.

It can be observed that the considered expressions fit the results well, the values of R^2 obtained for each model considered for both specimen is adequate (bigger than 86%). The average parameters obtained for the models fitted to the results are presented:

- Linear: $E = 23113.09$ Pa
- Neo-Hookean: $\mu = 14445.55\ N/m^2$;
- 2 parameter Mooney-Rivlin: $C_{10} = 9831.74$ Pa; $C_{01} = -4556.83$ Pa;

5.2 Deformation Simulations

In this part of the simulation the goal is to study the behaviour of the elastomer as a function of an applied force. This is achieved through the data of applied force on the indenter in relation to its displacement as it pushes on the elastomer. The indenter is modeled after the force sensor which was used to apply the force experimentally (Figure 5.3). To obtain the data experimentally, the force sensor is placed orthogonally to the top-most face of the *EcoFlex* part and lowered by increments of $\approx 55\mu m$ until it reaches $\approx 4400\mu m$, exerting a normal force on the *Ecoflex*. The simulation was modelled after this experiment.

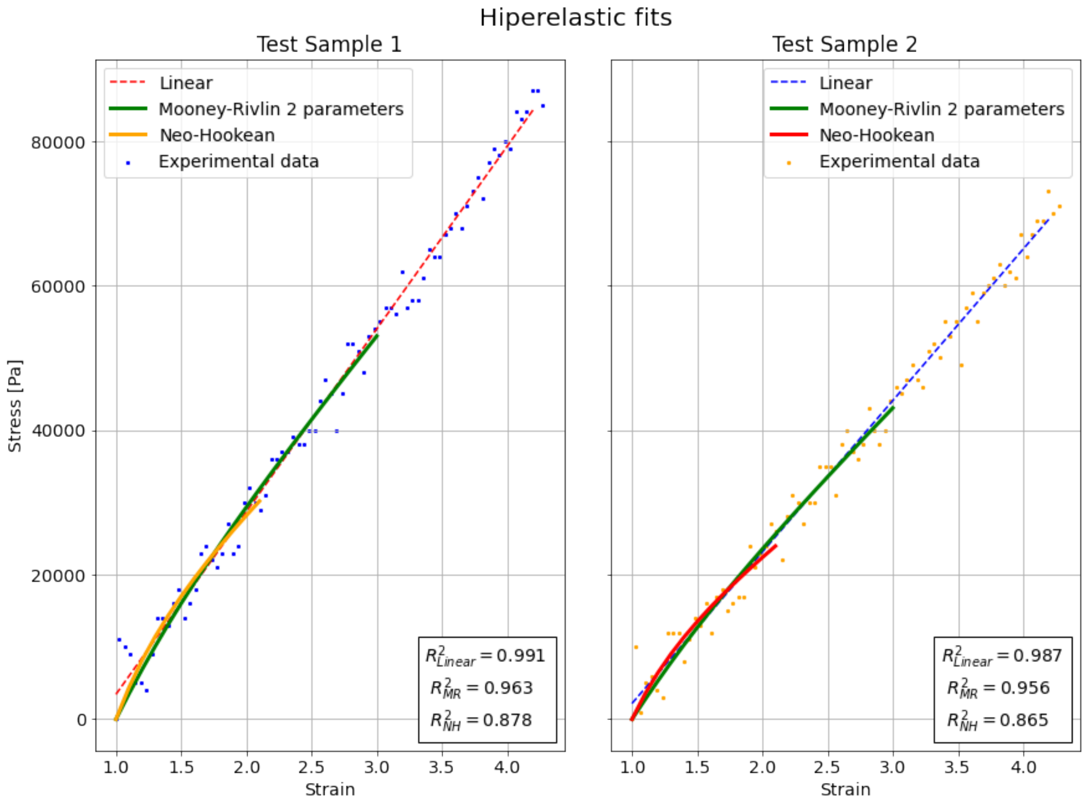

Figure 5.2: Experimental uniaxial traction test results and fitted models for both tensile specimen of pure *EcoFlex*.

Using the deformed mesh it is then, in theory, possible to obtain the position of the magnets and hence the magnetic field at the TMR sensors positions, which will be studied in the second part of this chapter.

For this simulation, the *COMSOL Multiphysics 5.5* structural mechanics module was used. The geometry of the *EcoFlex* piece was imported from a CAD drawing which was also used in the fabrication of the elastomer pieces used for experimental tests. The structures were meshed using the general physics tetrahedral mesh set to the fine mesh parameters.

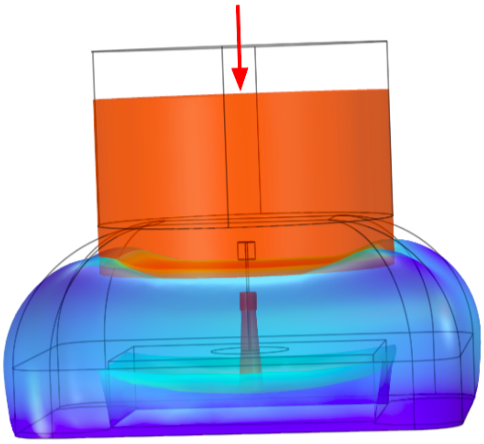

Figure 5.3: Deformation of *EcoFlex* piece by indenter.

5.2.1 Deformation models

Several material deformation models are tested in the simulations of the deformation of the pieces. These are described below.

Linear elastic model

A linear model is used first to simulate the deformation behaviour of the elastomer. For a linearly elastic material, the following relation applies:

$$\epsilon = \frac{1}{2}(\nabla u + \nabla u^T) \tag{5.1}$$

where ϵ is the strain tensor and u is the displacement vector. Using this model, the Young's Modulus and Poisson ration are sufficient to describe the elastic behaviour, assuming the material is isotropic.

Hyperelastic Model

As previously referred in 2.3 the behaviour of hyperelastic materials can be explained by the Generalized Rivlin Model, which relates the strain energy density of a material to the deformation gradient in the following manner, for incompressible materials:

$$W = \sum_{i,j=0}^{n} C_{ij}(I_1 - 3)^i (I_2 - 3)^j \tag{5.2}$$

In the Mooney-Rivlin of 2 parameters W is given by:

$$W = C_{10}(I_1 - 3) + C_{01}(I_2 - 3) \tag{5.3}$$

On the other hand, for the Mooney-Rivlin model of 5 parameters:

$$W = C_{10}(I_1 - 3) + C_{01}(I_2 - 3) + C_{20}(I_1 - 3)^2 + C_{02}(I_2 - 3)^2 + C_{11}(I_1 - 3)(I_2 - 3) \tag{5.4}$$

In the Mooney-Rivlin models, the C_{ij} are empirical constants.

Finally, in the limit $C_{ij \neq 10} = 0$, the Mooney-Rivlin model is reduced to the Neo-Hookean model:

$$W = C_{10}(I_1 - 3) \tag{5.5}$$

this relation applies to incompressible materials. When the material is not incompressible, a new constitutive constant other than C_{10} exists: D_1. Both of these can be estimated by the linear consistency formulas:

$$\begin{aligned} C_{10} &= \frac{\mu}{2} \\ D_1 &= \frac{k}{2} \end{aligned} \tag{5.6}$$

where μ is the shear modulus and k is the bulk modulus of the material. These can be calculated knowing only the Poisson ratio (ν) and Young's Modulus (E) of the material:

$$\begin{aligned} \mu &= \frac{E}{2(1+\nu)} \\ k &= \frac{E}{3(1-2\nu)} \end{aligned} \tag{5.7}$$

The results obtained are presented in Figure 5.4 in the form of on plot of the force applied on the pieces in relation to the displacement of the indenter comparing experimental and simulated cases, for the best fitting models obtained through simulations.

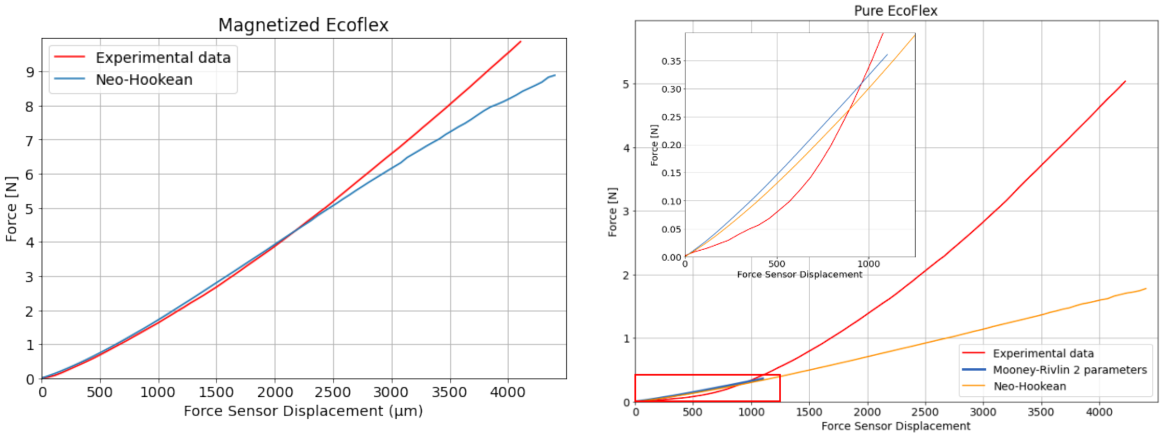

(a)

(b)

Figure 5.4: Displacement of indenter into pieces vs Force plots.

One can see that for the magnetized *EcoFlex* pieces, taking the experimental value as reference, the Neo-Hookean model presents a maximum error of the order of 15% for bigger deformations, which still constitutes a good result for FEM simulations.

As for the pure *EcoFlex* pieces, one can see that even for the the smaller deformations, the error is still too big for any of the models used (around 35% for the Neo-Hookean model). It is also evident that none of the two models considered behaves similarly to the experimental case, which means that a good FEM simulation was not achieved in this case. This can be due to several factors, such as the incomplete description of the mechanical properties provided by the uniaxial traction tests, the intrinsic errors of FEM simulations and the fact that the elastomer used was an old batch, which was noted to have different mechanical properties than newer batches.

It is also worthy of mention that, although only one ”type” of force was simulated in this work, it is possible to do so for many more possibilities of forces.

5.3 Permanent Magnet and Distributed Magnetization Simulations

In order to complete the simulations of the designed sensors, one should import the deformed mesh from the deformation simulation to another study in COMSOL. These deformed mesh could be used to simulate the magnetic behaviour in the TMR sensors positions. One would use the “Magnetic Fields, No Currents” physics from the AC/DC module and define the magnetization of the magnets by calculating their angle of rotation manually for each iteration using the “Measure” tool in the case of the pieces with permanent magnets. In the case of the magnetized pieces, since COMSOL does not allow for the simulation of magnetization in deformable materials, it would be necessary to export the displacement data and hard code the simulation. Approximating the angle of rotation of each point using the displacement of adjacent points, and using Equation 2.5 to find the magnetic field created by an arbitrary volume in a certain point, it would be possible to obtain an estimation for the magnetic field in the sensors positions.

Since the electronics data acquisition board used to acquire the output data of the sensors does not allow to retrieve the voltage (and hence the magnetic field) output due to arbitrary offsets introduced by the amplifiers, the only available data is in the form of ADC counts. Because of this it would not be possible to validate the simulation data. Due to this fact and to time constraints it was not possible to realize this part of the work.

5.3.1 SQUID measurement results

Despite what is described above, SQUID measurements were performed on the magnetized elastomer samples as described in Section 3.5. The results are presented in the plot in Figure 5.5, including the coercive magnetic field and the remanent magnetization, which are relevant to realizing the simulations.

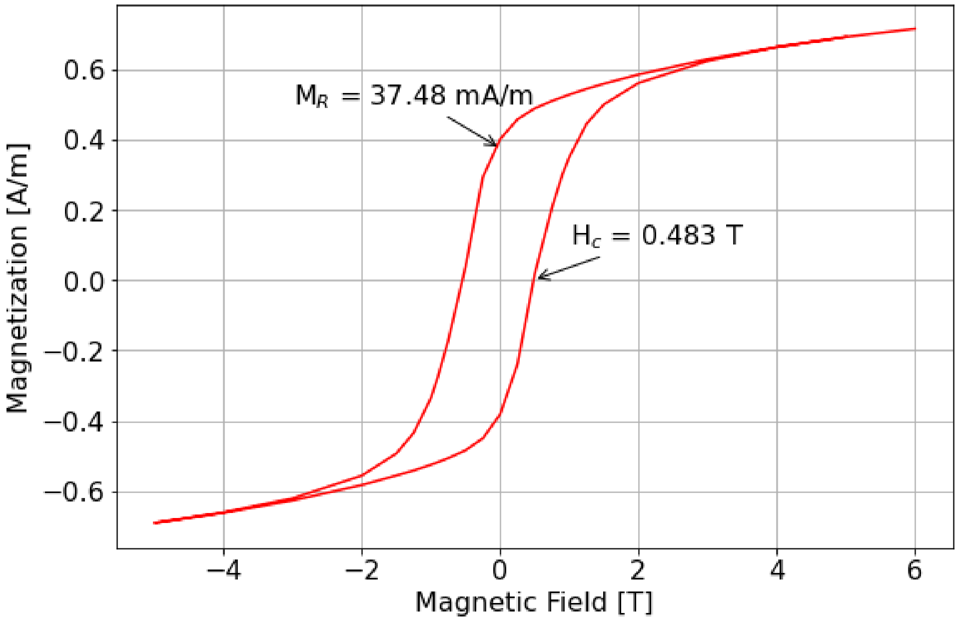

Figure 5.5: SQUID measurements for *Ecoflex* magnetized with magnetic particles in a 40:60 mass ratio.

Chapter 6

Results

In this chapter, the results of this thesis are presented. These include results from the characterization of the TMR sensors and also from the characterization and experimentation tests performed on the flexible tactile sensor design developed.

The magnetotransport curves for the TMR sensors fabricated are first presented and discussed, as well as their MR% ratio and other relevant quantities and then the results of the stability tests for the designed sensor are given. The final part of this chapter is dedicated to demonstrate how the designed sensor is capable of detecting both position and force intensity for normal forces with great accuracy by using machine learning algorithms.

6.1 TMR sensors characterization

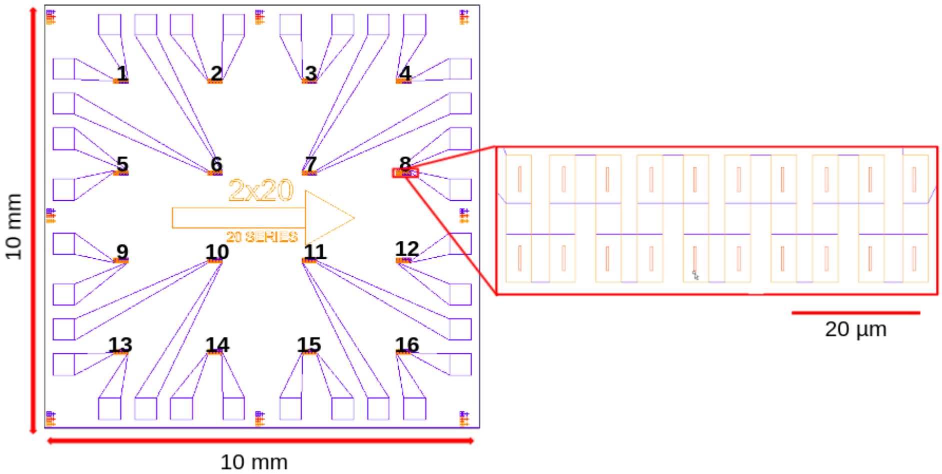

Figure 6.1: CAD mask used for the fabrication of the TMR sensors with numbered sensors (left) and CAD mask detail of a single sensor comprised of 20 MTJs connected in series (right)

In Chapter 3 the fabrication of the TMR sensors used in this work was described. After the fabrication process, the 4×4 TMR sensor die was mounted on a chip carrier and wirebonded. The chip carrier was ultimately connected to the electronic data acquisition board made by Fabian Naff of INESC-ID, to allow the sensors output data to be obtained.

As said before, each die fabricated consists of 16 TMR sensors, distributed in a 4×4 matrix configuration. Each TMR sensor consists in an array of 20 MTJs with an area of $20 \times 2\ \mu m^2$ connected in series.

In Figure 6.1, the CAD mask used in the fabrication of the TMR sensors is represented. The mask for one die is shown and also for one single sensor.

As described in Section 3.3.1, using the 140 Oe setup, the magnetotransport curves were taken for each sensor. An example of such a curve for one of the TMR sensors is presented in Figure 6.2.

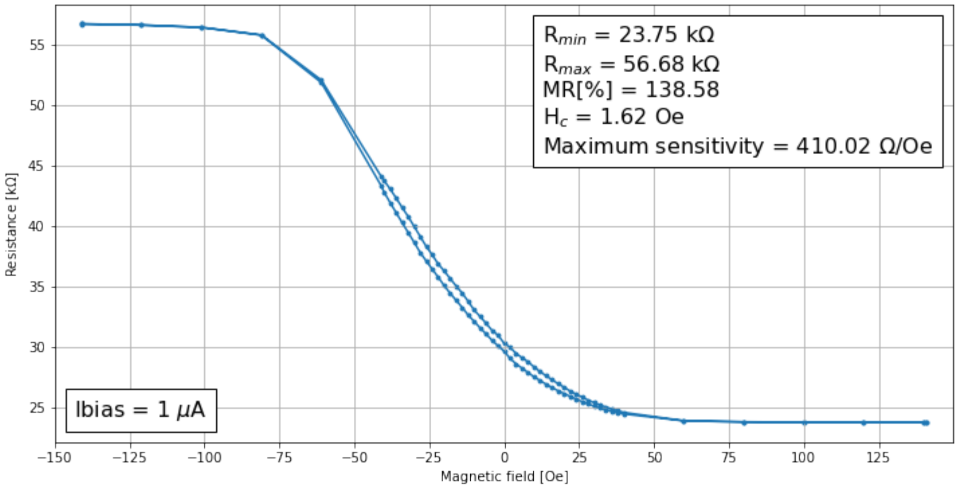

Figure 6.2: Example magnetotransport curve for sensor 1 with relevant parameters.

The plot shown is respective to one of the TMR sensors in the used die. The other sensors responses are similar, the maximum sensitivity varies in the range of [385.30 Ω/Oe, 561.25 Ω/Oe] which are good sensitivity values for the application at hand. As for the MR[%] it varies in the range of [116.68,142.85] which are normal values for MgO barrier MTJs. It is observed that the magnetotransport curve is not centered around the zero value of magnetic field as it is supposed to.

It is mentioned again that, although the output signal acquired using the data acquisitions board is proportional to the output voltage of each TMR sensors, calculating this voltages is impossible because the proportion is unknown due to the random offsets introduced by the amplifiers in the acquisition board. Hence, the output of the sensors was acquired and is subsequently shown always in Analog to digital converter (ADC) counts. ADCs convert analog signals, such as voltage, to 12 bit digital signals. In this work, a successive approximation ADC uses a binary search algorithm to converge upon a 12 bit signal that when converted to analog using a DAC (digital to analog converter) is equal to the original analog signal. Since the TMR sensor signal that reaches the ADC in this thesis is already biased by the non deterministic amplifier offsets, it is only possible to obtain the voltage converted by the ADC and not the voltage output of the sensor.

6.2 Sensor Stability test

After characterizing the TMR sensors magnetically, the next step was to experimentally test the designed sensor in force sensing and recognition using the setup described in Section 3.3.2. The chip carrier with the TMR sensors was then mounted on the INESC-ID designed electronics acquisition board and connected to a computer. The stability test as was then performed and stability evaluated for each TMR sensor. It consisted in using the force sensor as an indenter and move it down until it was approximately 3500 μ into the *EcoFlex* piece for 3 seconds and then move it up until the force applied on the elastomer piece was zero for another 3 seconds. The results of this test are summarized in Figure 6.3.

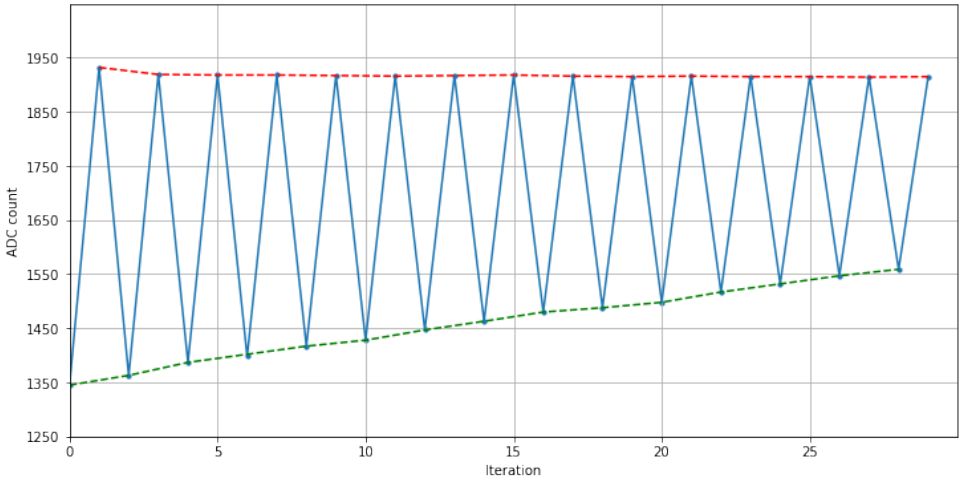

Figure 6.3: TMR sensor output vs iteration of experiment. Each point is the average of 3 seconds of acquisition and an iteration represents a step of moving the sensor up/down.

In this plot, each iteration represents a step of lowering or lifting the force sensor into or from the elastomer piece. The points represent the average taken of the output of the sensor during the 3 seconds of each step as acquired with the acquisition board. Due to the similarity between the behaviour of all the TMR sensors in these experiment, the stability plot of only one TMR sensor is presented.

As one can observe, the response of the sensor when the elastomer piece is not being actuated on, represented in the plot by the red dashed line, is very constant from which can be concluded that there is not a biasing in the sensors, that is, for the same force applied on the elastomer (0N in this case), the sensors output the same result. This means that the change of the magnetic field is completely reverted after a deformation of the piece, thus it can be inferred that the *EcoFlex* piece comes back to its initial form even after large deformations.

As for the points corresponding to when there is a force applied on the elastomer, we notice a clear upwards trend, this is explained by the precision stage moving a distance which is a little bit different than the one ordered in each iteration, which causes it to move into the elastomer piece a little less each time, thus applying a smaller force. So, this has nothing to do with the stability of the sensor or lack there of.

6.3 Force intensity and location sensing

Since the output voltage of the sensors was impossible to calculate, it was impracticable to obtain the voltage vs magnetic field characteristic of the sensors. With this in mind, the ADC counts output was used to analyze the capabilities of the designed sensor in detecting the intensity and position of normal forces.

The data analyzed was acquired by the following procedure: in 5 different application points, a normal force was applied by a 3D printed indenter that allows for the force to be applied in a much smaller application point was fitted in the force sensor (the indenter and application points are shown in Figure 6.4). The normal force was applied by moving the force sensor until it was directly above the application point and at the same height as the surface of the elastomer piece in that point. 81 steps were then made where the force sensor was moved $50\mu m$ down into the piece and the output of the 16 sensors saved in a file, as well as the output of the force sensor and a number that serves as an identifier of the application point (also shown in Figure 6.4, in the figure is also represented the sensitive direction of the sensors by the red arrow).

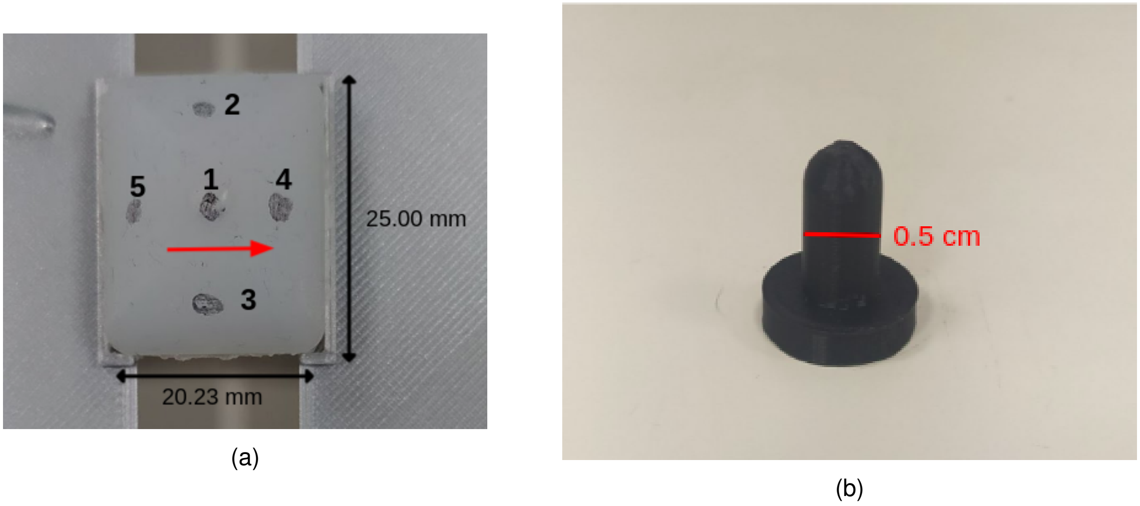

(a)

(b)

Figure 6.4: *EcoFlex* piece with the different application points marked on its surface (left). indenter used to apply the forces (right).

To analyze the data obtained from this a simple machine learning model was trained. For the estimation of the intensity of the force, a Random Forest regression was used. Random forest is a supervised learning algorithm that works by constructing various decision trees which are created from a different sample of rows. Each tree makes its individual prediction and in the end the predictions of all the trees are averaged to obtain a single result. The way decision trees work is by dividing a dataset (represented by a root node) into smaller subsets which are homogeneous (contain similar data) and as heterogeneous as possible between each other. The criteria for the split can be, for example, the mean squared error value. The splitting ends when it reaches a limit imposed or when the terminal nodes (”leafs”) only have on instance in them and it is impossible to split more, having then reached a decision.

In this work, the number of decision trees used in the Random forest regression was 100. Since not many data points were acquired in the experiments, a cross-validation strategy was used to estimate the performance of the model. The leave one out cross-validation strategy was used, which consists in dividing the data into a number of subsets which is equal to the number of points in the whole dataset. After the division, each subset will take turns being used as the test set while all the other examples are used as the training set. So, this strategy fits and evaluates as many models as the number of points gathered. This allows to have better estimates of the performance of the model on the dataset in question by averaging scores such as the mean absolute error. This method of cross-validation is very computationally expensive, which is why it is not used unless in small datasets.

This model was trained and fitted into the data gathered for the 5 application points for all the different types of *EcoFlex* pieces. The inputs of the model are the ADC counts obtained from each of the 16 TMR sensors. In Figure 6.5 the plots of the true force versus the estimated force values are presented.

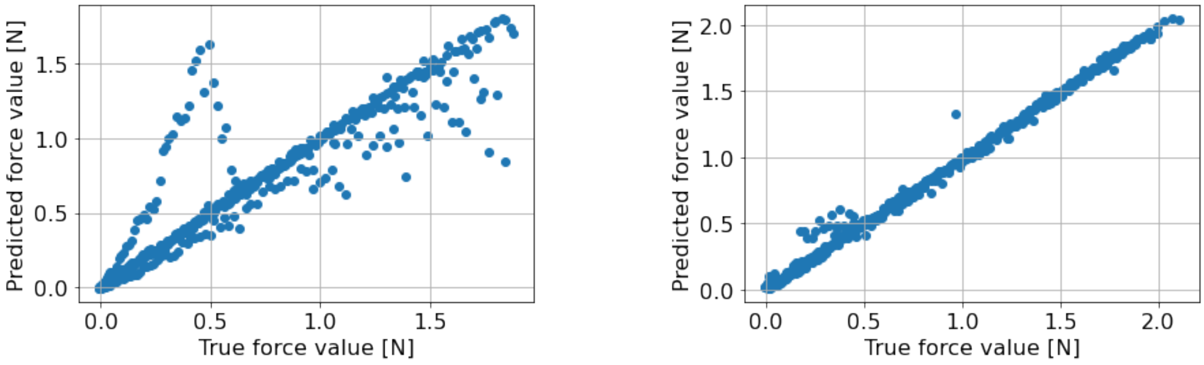

(a) *EcoFlex* piece with 1 permanent magnet.

(b) *EcoFlex* piece with 5 permanent magnets.

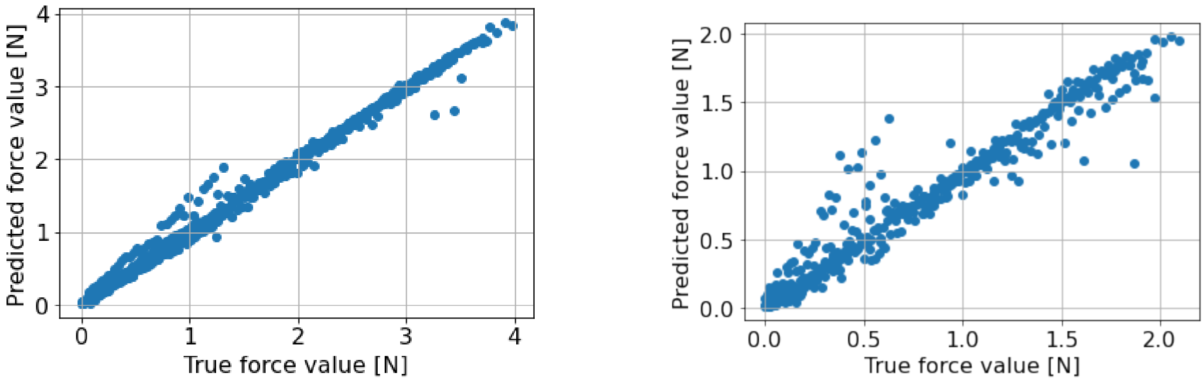

(c) *EcoFlex* piece homogeneously magnetized with magnetic particles.

(d) *EcoFlex* piece with 5 magnetic particle ”islands”.

Figure 6.5: Estimated versus true force plots for each *EcoFlex* piece.

As can be observed, the model generally estimates the force quite well, especially for the *EcoFlex* pieces with 5 permanent magnets and with distributed magnetization. The values of the force estimated by the model are very close to the values measured experimentally (true values), with few outliers. As for the elastomer pieces with 1 permanent magnet and with magnetic particle ”islands”, the model does not work quite as well, with a high number of outliers (especially for the case with one permanent magnet) and a higher error than in other cases (in the case of the magnetic particle ”islands”), as can

	1 PM	5 PM	Distributed MPs	MP islands
R^2	0.835	0.993	0.988	0.940
MAE [N]	0.101	0.027	0.069	0.083

Table 6.1: R^2 and mean absolute error for the regression model, for each configuration of the *EcoFlex* pieces.

be observed by the MAE (mean absolute error) values in Table 6.1. MAE can be defined as the mean absolute difference between the estimate and the real value of the force, as given by the expression:

$$MAE = \frac{\sum_{i=1}^{n} EF_i - TF_i}{n} \tag{6.1}$$

where EF_i is the force estimate given by the model used and TF_i is the true force value obtained experimentally.

It is worthy of mention that a bias seems to exist in the force estimates, since there appears to be a pattern in the outliers over the 4 elastomer configurations, their distribution does not look totally random.

One can observe that the results for the case of the elastomer piece with homogeneously distributed magnetic particles are very good, despite the magnetic noise that arises from having a piece magnetized in its entirety. This can be explained by the fact that, since there is magnetic field produced in every point in the piece, the MF deformation will be produced with higher intensity in the point of application of the force and therefore it will influence the closest TMR sensors to a higher degree. This doesn't happen, for example, in the magnetic particle ”islands” case, where the deformation of MF is always produced on the magnetized ”islands”.

The higher values of MAE and lower R^2 for the one permanent magnet case, might be explained by the fact that the magnetic field comes only from one point in the elastomer piece, which makes it difficult to determine through just the output of the sensors the intensity of the force, especially when it is exerted in the same ranges for all of the 5 application points. This difficulty is augmented by the fact that each sensor is only sensitive to one direction of magnetic field, which is the same for every TMR sensor.

In the case of the elastomer piece with the magnetic particle islands, an explanation for the bigger MAE might be that the application points of the force coincide with the position of the ”islands”. Besides this they are symmetrical in pairs in relation to the x and y axes, which might cause the changes of the magnetic field to cancel a bit when a force is applied since two of them will deform in opposite directions.

The next step was to estimate the position of the force. Since there are only 5 application points, a regression estimator would have increased difficulty trying to predict the exact position of the force outside these 5 points because there are no data for it to interpolate. Thus, the strategy was to use attribute a class to each application point and check if a classifier could distinguish between the different application points. The labels of the classes correspondent to each application point are the numbers present besides them in Figure 6.4.

A support vector machine (SVM) classifier with polynomial kernel was used in this step. This is a supervised learning algorithm that takes data points and outputs the hyperplane that best separates the classes. The idea behind it is to maximize the distance of the hyperplane to the nearest element of every class. It is very useful to classify nonlinear data, it does this by mapping this data to higher dimensions where the data is linearly separable and then mapping it back to the original space. Similar to the estimation of the intensity of the force, the model was trained and fit to the data and the leave one out cross-validation strategy was also used here to better estimate the performance of the model. The inputs of the model are the ADC counts obtained from each of the 16 TMR sensors. The confusion matrixes for each of the 4 pieces of elastomer are presented in Figure 6.6.

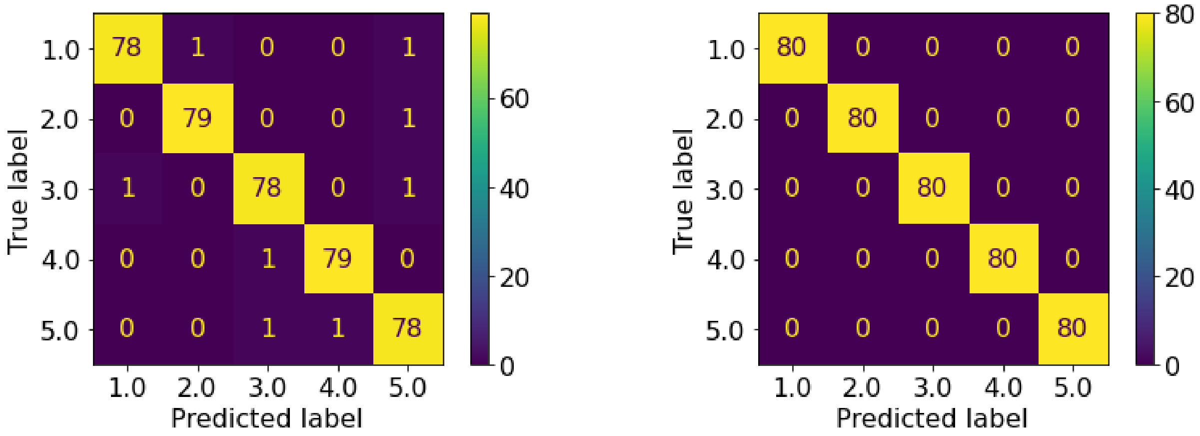

(a) *EcoFlex* piece with 1 permanent magnet.

(b) *EcoFlex* piece with 5 permanent magnets.

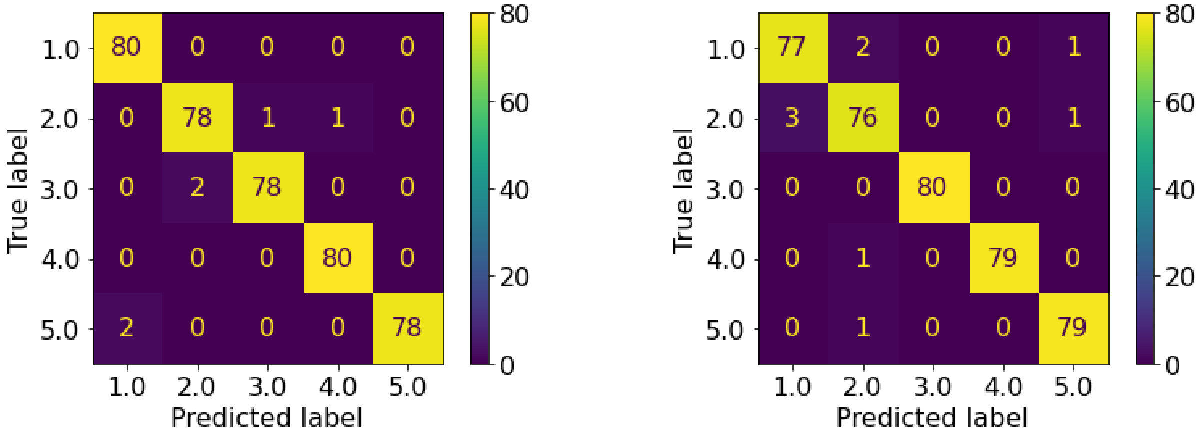

(c) *EcoFlex* piece magnetized with magnetic particles.

(d) *EcoFlex* piece with 5 magnetic particle ”islands”.

Figure 6.6: Confusion matrixes for each *EcoFlex* piece.

	1 PM	5 PM	Distributed MPs	MP islands
Accuracy	0.98	1.00	0.98	0.97

Table 6.2: Accuracy of classifier for each elastomer piece.

As can be observed by the confusion matrixes, the SVM classifier is very accurate in estimating the class of data, with almost 100% accuracy in every elastomer piece. The calculated accuracies for each of them are presented in the Table 6.2.

Finally, because the estimation of the force had an high MAE for the elastomer piece with one permanent magnet and also, at a lesser degree, for the piece with magnetic particle ”islands”, the same random forest regression model was used to estimate the force, but this time assuming the class was already known (by giving the class as an input to the model as well). The experimental versus estimated force plots are presented in Figure 6.7 for the two pieces considered.

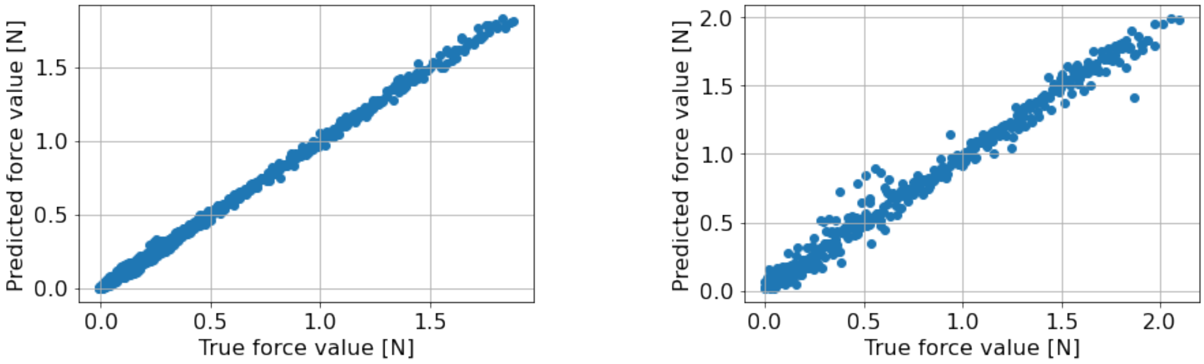

(a) *EcoFlex* piece with one permanent magnet.

(b) *EcoFlex* piece with 5 magnetic particle ”islands”.

Figure 6.7: Estimated versus true force plots for each *EcoFlex* piece considered.

By comparing the two plots with the first ones obtained without considering the class an input, the improvement is evident. The MAE for both the situations lowers as there are also less outliers and the R^2 value improves, as can be seen in Table 6.3. The bias that was previously noted has also disappeared. This results are an indication that the if the position of the force is calculated in the first place, the model will more accurately estimate the force afterwards.

	1 PM	MP islands
R^2	0.998	0.982
MAE [N]	0.020	0.053

Table 6.3: R^2 and mean absolute error for the regression model for both situations considered.

Chapter 7

Conclusions

The work developed in this thesis had the goal of developing a tactile sensor capable of detecting forces and their locations through a simple setup. The sensor was designed as a magnetized artificial flexible skin using *EcoFlex*, with a 4×4 matrix of TMR sensors, all with the same sensing direction, used to detect the changes in magnetic field when a force deformed the magnetized elastomer piece.

A FEM simulation model was developed to simulate the behaviour of the sensor, namely the voltage vs magnetic field characteristic of the sensor, by mimicking the physical parameters of the system at hand. An uniaxial tensile test was performed on both homogeneously magnetized *EcoFlex* (60:40 mass ratio of *EcoFlex*:MPs) and pure *EcoFlex* specimens to obtain their strain vs stress curve and fit to several material models to obtain their parameters in order to use them in the simulation model. The first part of the simulation, the deformation simulation, was successful in describing the deformation of homogeneously magnetized *EcoFlex*, which was validated against experimental force data acquired, with a maximum error of approximately 15% for the whole deformation domain. However, it failed to do so for pure *EcoFlex*. As previously mentioned this might be due to various factors such as the fact that performing only uniaxial traction testing gave an incomplete description of the mechanical properties of the material, or even due to the fact that the *EcoFlex* used in these specimen was an old batch which was noted to have different mechanical properties than newer batches.

The second part of the simulation, which was calculating the magnetic field in the TMR sensors locations when a force is applied on the elastomer, was not realized due to time constraints and the fact that the software used does not support the multiphysics needed to perform it. Future work would include performing this part of the simulation. However, SQUID magnetometer measures were taken of homogeneously magnetized *EcoFlex*, giving a calculated value of $M_R = 37.48mA/m$.

The fabricated sensors were tested to determine their electrical stability and the ability to differentiate force intensity and localization. Four different sensors were tested, being the difference in the *EcoFlex* pieces used as the source of the stray field for the TMR sensors to detect. Due to the offsets imposed by the amplifiers in the acquisition electronics board, it was impossible to calculate the voltage output of the sensors, so all the work had to be done in ADC counts.

The *EcoFlex* proved very stable when being actuated repeatedly during 30 iterations between a fixed deformation and no deformation, giving a constant ADC counts output for the same force applied.

By using a random forest regression model, all the sensor configurations were also able to estimate the intensity of normal forces with a good fit to the model and a low mean absolute error of approximately 0.1N for the *EcoFlex* with one permanent magnet, 0.02N for the one with 5 permanent magnets, 0.07 for the homogeneously magnetized *EcoFlex* configuration, and 0.08 for the configuration with magnetic particle ”islands”. Although the first and last mentioned had a value of R^2 slightly lower than the other two.

It was then proved the ability of the sensors to differentiate between 5 different points of application of the forces, by using a support vector machine classifier, with a minimum accuracy over configurations of 0.97.

Future work would include, in short term, the acquisition of more force data over all the area of the *EcoFlex* pieces with the goal of generalizing the estimation of the location of the forces applied. Also compression tests should be made on *EcoFlex* test specimen to improve the fit of the deformation models to the results and thus obtaining better parameters for the simulations. Finally, a good addition to the work already realized would be to fabricate a new electronics acquisition board, that would allow for the calculations of the voltage output of the sensors and therefore the determination of the force vs magnetic field characteristic.

Bibliography

[1] B. D. Argall and A. G. Billard. A survey of tactile human–robot interactions. *Robotics and Autonomous Systems*, 58(10):1159–1176, 2010. ISSN 0921-8890. doi: https://doi.org/10.1016/j.robot.2010.07.002.

[2] A. Alfadhel and J. Kosel. Magnetic nanocomposite cilia tactile sensor. *Advanced Materials*, 27(47): 7888–7892, 2015.

[3] G. Cannata, M. Maggiali, G. Metta, and G. Sandini. An embedded artificial skin for humanoid robots. In *2008 IEEE International Conference on Multisensor Fusion and Integration for Intelligent Systems*, pages 434–438, 2008. doi: 10.1109/MFI.2008.4648033.

[4] X. Wang, T. Xu, S. Dong, S. Li, L. Yu, W. Guo, H. Jin, J. Luo, Z. Wu, and J. M. King. Development of a flexible and stretchable tactile sensor array with two different structures for robotic hand application. *RSC Adv.*, 7:48461–48465, 2017. doi: 10.1039/C7RA08605A. URL `http://dx.doi.org/10.1039/C7RA08605A`.

[5] C. Chi, X. Sun, N. Xue, T. Li, and C. Liu. Recent progress in technologies for tactile sensors. *Sensors*, 18(4), 2018. ISSN 1424-8220. doi: 10.3390/s18040948. URL `https://www.mdpi.com/1424-8220/18/4/948`.

[6] M. I. Tiwana, S. J. Redmond, and N. H. Lovell. A review of tactile sensing technologies with applications in biomedical engineering. *Sensors and Actuators A-physical*, 179:17–31, 2012.

[7] R. S. Dahiya, L. Lorenzelli, G. Metta, and M. Valle. Posfet devices based tactile sensing arrays. In *Proceedings of 2010 IEEE International Symposium on Circuits and Systems*, pages 893–896, 2010. doi: 10.1109/ISCAS.2010.5537414.

[8] P. S. Girão, P. M. P. Ramos, O. Postolache, and J. Miguel Dias Pereira. Tactile sensors for robotic applications. *Measurement*, 46(3):1257–1271, 2013. ISSN 0263-2241. doi: https://doi.org/10.1016/j.measurement.2012.11.015. URL `https://www.sciencedirect.com/science/article/pii/S0263224112004368`.

[9] K. Weiss and H. Worn. The working principle of resistive tactile sensor cells. *IEEE International Conference Mechatronics and Automation, 2005*, 1:471–476 Vol. 1, 2005.

[10] D. Sartiano and S. Sales. Low cost plastic optical fiber pressure sensor embedded in mattress for vital signal monitoring. *Sensors*, 17(12), 2017. ISSN 1424-8220. doi: 10.3390/s17122900. URL `https://www.mdpi.com/1424-8220/17/12/2900`.

[11] L. Jamone, L. Natale, G. Metta, and G. Sandini. Highly sensitive soft tactile sensors for an anthropomorphic robotic hand. *IEEE Sensors Journal*, 15:4226–4233, 2015.

[12] P. Gazda and R. Szewczyk. Novel giant magnetoimpedance magnetic field sensor. *Sensors*, 20 (3), 2020. ISSN 1424-8220. doi: 10.3390/s20030691. URL `https://www.mdpi.com/1424-8220/20/3/691`.

[13] D. Silvera-Tawil, D. Rye, and M. Velonaki. Artificial skin and tactile sensing for socially interactive robots: A review. *Robotics and Autonomous Systems*, 63:230–243, 2015. ISSN 0921-8890. doi: https://doi.org/10.1016/j.robot.2014.09.008. Advances in Tactile Sensing and Touch-based Human Robot Interaction.

[14] J. Dargahi and S. Najarian. Human tactile perception as a standard for artificial tactile sensing—a review. *The international journal of medical robotics + computer assisted surgery : MRCAS*, 1: 23–35, 11 2004. doi: 10.1002/rcs.3.

[15] S. Sundaram, P. Kellnhofer, Y. Li, J.-Y. Zhu, A. Torralba, and W. Matusik. Learning the signatures of the human grasp using a scalable tactile glove. *Nature*, 569(7758):698–702, 2019.

[16] G. Cannata, M. Maggiali, G. Metta, and G. Sandini. An embedded artificial skin for humanoid robots. *2008 IEEE International Conference on Multisensor Fusion and Integration for Intelligent Systems*, pages 434–438, 2008.

[17] C.-H. Chuang, W.-B. Dong, and W.-B. Lo. Flexible piezoelectric tactile sensor with structural electrodes array for shape recognition system. pages 504 – 507, 01 2009. doi: 10.1109/ICSENST.2008.4757157.

[18] Y. Ohmura, Y. Kuniyoshi, and A. Nagakubo. Conformable and scalable tactile sensor skin for curved surfaces. volume 2006, pages 1348 – 1353, 06 2006. doi: 10.1109/ROBOT.2006.1641896.

[19] Y. Yan, Z. Hu, Z. Yang, W. Yuan, C. Song, J. Pan, and Y. Shen. Soft magnetic skin for super-resolution tactile sensing with force self-decoupling. *Science Robotics*, 6(51):eabc8801, 2021.

[20] T. Hellebrekers, O. Kroemer, and C. Majidi. Soft magnetic skin for continuous deformation sensing. *Advanced Intelligent Systems*, 1(4):1900025, 2019.

[21] J. Coey and J. Coey. *Magnetism and Magnetic Materials*. Knovel Library. Cambridge University Press, 2010. ISBN 9780521816144.

[22] S. Abrunhosa. Magnetoresistive sensors for industrial positioning applications. Master's thesis, Insituto Superior Técnico, 2018.

[23] M. Julliere. Tunneling between ferromagnetic films. *Physics Letters A*, 54(3):225–226, 1975. ISSN 0375-9601. doi: https://doi.org/10.1016/0375-9601(75)90174-7.

[24] J.-G. J. Zhu and C. Park. Magnetic tunnel junctions. *Materials Today*, 9(11):36–45, 2006. ISSN 1369-7021. doi: https://doi.org/10.1016/S1369-7021(06)71693-5.

[25] A. V. Silva, D. C. Leitao, J. Valadeiro, J. Amaral, P. P. Freitas, and S. Cardoso. Linearization strategies for high sensitivity magnetoresistive sensors. *European Physical Journal-applied Physics*, 72: 10601, 2015.

[26] M. A. Ruderman and C. Kittel. Indirect exchange coupling of nuclear magnetic moments by conduction electrons. *Phys. Rev.*, 96:99–102, Oct 1954. doi: 10.1103/PhysRev.96.99. URL `https://link.aps.org/doi/10.1103/PhysRev.96.99`.

[27] S. S. P. Parkin and D. Mauri. Spin engineering: Direct determination of the ruderman-kittel-kasuya-yosida far-field range function in ruthenium. *Phys. Rev. B*, 44:7131–7134, Oct 1991. doi: 10.1103/PhysRevB.44.7131. URL `https://link.aps.org/doi/10.1103/PhysRevB.44.7131`.

[28] K. Fujiwara, M. Oogane, F. Kou, D. Watanabe, H. Naganuma, and Y. Ando. Fabrication of magnetic tunnel junctions with a synthetic ferrimagnetic free layer for magnetic field sensor applications. *Japanese Journal of Applied Physics*, 50, 02 2011. doi: 10.1143/JJAP.50.013001.

[29] P. P. Freitas, R. Ferreira, S. Cardoso, and F. Cardoso. Magnetoresistive sensors. *Journal of Physics: Condensed Matter*, 19(16):165221, apr 2007. doi: 10.1088/0953-8984/19/16/165221. URL `https://doi.org/10.1088/0953-8984/19/16/165221`.

[30] P. Ribeiro. Ciliary structure inspired force sensor for robotic platforms. Master's thesis, Insituto Superior Técnico, 2016.

[31] S. Liao, S. Yuan, and H. Bertram. Biasing characteristics of unshielded, boundary exchange-coupled sal/mr sensors. *IEEE Transactions on Magnetics*, 29(6):3873–3875, 1993. doi: 10.1109/20.281327.

[32] J. DeWolf, D. Mazurek, F. Beer, and E. Johnston. *Mechanics of Materials*. McGraw-Hill Education, 2014. ISBN 9780073398235. URL `https://books.google.pt/books?id=pU0ungEACAAJ`.

[33] R. S. Rivlin and D. W. Saunders. Large Elastic Deformations of Isotropic Materials. VII. Experiments on the Deformation of Rubber. *Philosophical Transactions of the Royal Society of London Series A*, 243(865):251–288, Apr. 1951. doi: 10.1098/rsta.1951.0004.

[34] What is the difference between a hyperelastic material and an elastic material in recurdyn? `https://support.functionbay.com/en/faq/single/87/difference-hyperelastic-material-elastic-material-recurdyn`. Accessed: 2021-10-28.

[35] S. Cardoso, V. Gehanno, R. Ferreira, and P. Freitas. Ion beam deposition and oxidation of spin-dependent tunnel junctions. *IEEE Transactions on Magnetics*, 35(5):2952–2954, 1999. doi: 10.1109/20.801044.

[36] D. C. Leitão, J. P. Amaral, S. Cardoso, and C. Reig. *Microfabrication Techniques*, pages 31–45. Springer Berlin Heidelberg, Berlin, Heidelberg, 2013. ISBN 978-3-642-37172-1. doi: 10.1007/978-3-642-37172-1_2. URL `https://doi.org/10.1007/978-3-642-37172-1_2`.

[37] R. Varela. Optimization of MR Sensor Geometry Towards Picotesla Detection. Master's thesis, Insituto Superior Técnico, 2015.

[38] Reactive ion etching. `https://www.mksinst.com/n/reactive-ion-etching`. Accessed: 2021-09-12.

[39] J. H. Warner, F. Schäffel, A. Bachmatiuk, and M. H. Rümmeli. Chapter 4 - methods for obtaining graphene. In J. H. Warner, F. Schäffel, A. Bachmatiuk, and M. H. Rümmeli, editors, *Graphene*, pages 129–228. Elsevier, 2013. ISBN 978-0-12-394593-8. doi: https://doi.org/10.1016/B978-0-12-394593-8.00004-7.

[40] K. Halbach. Design of permanent multipole magnets with oriented rare earth cobalt material. *Nuclear Instruments and Methods*, 169(1):1–10, 1980. ISSN 0029-554X. doi: https://doi.org/10.1016/0029-554X(80)90094-4.

[41] Ecoflex™ 00-30. `https://www.smooth-on.com/products/ecoflex-00-30/`. Accessed: 2021-09-12.

[42] F/t sensor: Nano17. `https://www.ati-ia.com/products/ft/ft_models.aspx?id=Nano17`. Accessed: 2021-10-01.

[43] R. Ilmoniemi and R. Näätänen. Magnetoencephalography. In N. J. Smelser and P. B. Baltes, editors, *International Encyclopedia of the Social Behavioral Sciences*, pages 9131–9137. Pergamon, Oxford, 2001. ISBN 978-0-08-043076-8. doi: https://doi.org/10.1016/B0-08-043076-7/03411-2.

[44] T. Thomson. 10 - magnetic properties of metallic thin films. In K. Barmak and K. Coffey, editors, *Metallic Films for Electronic, Optical and Magnetic Applications*, pages 454–546. Woodhead Publishing, 2014. ISBN 978-0-85709-057-7. doi: https://doi.org/10.1533/9780857096296.2.454.

[45] Fitting measured data to different hyperelastic material models. `https://br.comsol.com/blogs/fitting-measured-data-to-different-hyperelastic-material-models/`. Accessed: 2021-10-22.

Appendix A

TMR sensors runsheet

Page intentionally left blank.

Runsheet – Multiproject Wafer #12

Process Start: 01/03/2021 **Process Finish:** 11/03/2021

Responsible: Maria Carvalho, Rita Macedo, Susana Freitas

STEP 0: *TMR Stack Deposition* *01/03/2021*

Sample ID: N88TJ153v4x_3226_CoFe_tune **Machine:** N3600/ N8800

Run # 3370

Stack: [Ta 5/Ru 10]x3/Ta 5/Ru 5/MnIr 8/CoFe 2.2/Ru 0.75/ CoFeB 1.9/ MgO 1.55/CoFeB 3/Ru 0.2/NiFe 4/Ru 5/Ta 5/Ru 10/ TiWN 30

Total Thickness (with TiWN): 126.6 nm

STEP 1: *TiWN Deposition* *01/03/2021*

Operator: Rita Macedo **Machine:** N3600

1.1 Target clean

Run: 3372 Sequence: TiWN_clean Time: 500 s

1.2 TiWN 30nm Dep

Run: 3373 Sequence: TiWN_30nm Dep. Rate: 0.4 Å/s

Function: Mod1 F91 Thickness: 30 nm Time: 375s

STEP 2: 1st *Lithography – Pillar (L1)* *01/03/2021*

Operator: Maria Carvalho **Machine:** DWL

1.1 Vapor Prime 30 min (Recipe – 0)

1.2 Coat 1.5 µm Photoresist

Recipe Name: 8 resist

1.2.1 Manual resist dispense: 9s @ 800rpm; 10000rpm/s
1.2.2 Spin: 27s @ 2800rpm; 20000rpm/s
1.2.3 Bake 60s @ 95°C

1.3 Lithography

Map: MPW8

Inverted mask

Mask: (\h1 partition)

MagID_T64V2_Pillars
MagID_RadialS_V5_Pillars
MagID_LineS_V1_Pillars
PR0603_Pillars
MPWs_stat_Pillar
Matrix_Pillar

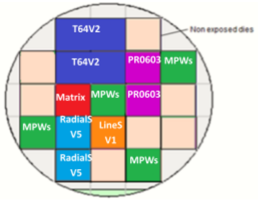

Energy: 75 **Focus:** -10 **Power:** 84

Die dimensions: MagID_RadialS/ MPW9: 22301 x 22200 µm
PR0603: 25400 x 25400 µm
MagID_LineS: 22301 x 16600 µm
MadID_T64V2: 50800 x 25400 µm
Matrix: 20000 x 20000 µm

 # Dies: 14 **Total Time:**

1.4 Develop

Recipe Name: 8develop

1.4.1 Bake 60s @ 110°C
1.4.2 Water rinse: 5s @ 500rpm; 10000rpm/s
1.4.3 Developer spray: 5s @ 500rpm; 5000rpm/s
1.4.4 Liquid developer: 2.1s @ 0rpm
1.4.5 Spin: 60s @ 0rpm
1.4.6 Water rinse: 15s @ 500rpm; 5000rpm/s
1.4.7 Spin: 40s @2000rpm; 20000rpm/s

Optical Inspection | Comments:

- Defined structures
- Structure's dimensions correct?

STEP 3: *MTJ Definition by Ion Milling* *02/03/2021*

Operator: Maria Carvalho e Rita Macedo **Machine:** N3600

Total stack thickness: 1266 Å **Thickness to etch:** 712 Å

Etch rates (for ref) 60º: 1.1 Å/s **Etch rate 30º:** 1.27 Å/s

Sequence name: Etch_junction_second

Time steps: 3*170'' @ pan = 60°

Time steps: 2*120'' @ pan = 30°

Extra etching steps (if necessary)

Time steps: ______________________________ @ pan = 60°

Time steps: ______________________________ @ pan = 30°

Base Pressure: ______________ Torr **Run #** 3388

Conditions:

Assist Gun		**Power (W)**	**V+ (V)**	**I+ (mA)**	**V- (V)**	**I- (mA)**	**Ar Flux (sccm)**	**W.P. (Torr)**
Set Point		180	650	-	350	-	16	-
Read Values	**60°**	180/2	657	104	348	3	15.9	1.25×10^{-4}
	30°	180/2	656	104	348	4	15.9	1.24×10^{-4}

Neutralizer: 0 mA/ 3 sccm

Inspection | Comments

- Burnt resist No
- Profilometry test structure: ΔMTJ = 777 Å

STEP 4: Resist Ashing *02/03/2021*

Operator: Maria Carvalho **Machine:** SPTS

Recipe: O2_Ashing_15mTorr_240s

Conditions:

	P_{source} (W)	**VP-P_{source} (V)**	**P_{platen} (W)**	**VP-P_{platen} (V)**	**APC (%)**	**O_2 Flux (sccm)**	**Pressure (mTorr)**	**He Press. (Torr)**
Set point	600	-	30	-		95	15	15
Read Values	601/2	2521	30/4	261	8	95	15	15

Optical Inspection | Profilometry | Comments

- Burnt resist No
- More ashing needed? How much: No
- Step height

STEP 5: 2nd *Lithography – Bottom electrode Definition (L2)* *02/03/2021*

Operator: Maria Carvalho **Machine:** DWL

1.1 Vapor Prime 30 min (Recipe – 0)

1.2 Coat 1.5 µm Photoresist

Recipe Name: 8 resist

1.2.1 Manual resist dispense: 9s @ 800rpm; 10000rpm/s
1.2.2 Spin: 27s @ 2800rpm; 20000rpm/s
1.2.3 Bake 60s @ 95°C

1.3 Lithography

Map: MPW8

Inverted mask

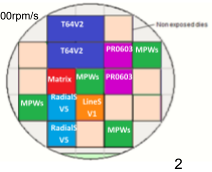

Mask: (\h1 partition)

MagID_T64V2_ Bottom
MagID_RadialS_V5_ Bottom
MagID_LineS_V1_ Bottom
PR0603_ Bottom
MPWs_stat_Bottom
Matrix_Bottom

Energy: 80 **Focus:** -10 **Power:** 84

 # Dies: **Total Time:** 5h

Alignment cross marks: see last page

1.4 Develop

Recipe Name: 8develop

1.4.1 Bake 60s @ 110°C
1.4.2 Water rinse: 5s @ 500rpm; 10000rpm/s
1.4.3 Developer spray: 5s @ 500rpm; 5000rpm/s
1.4.4 Liquid developer: 2.1s @ 0rpm
1.4.5 Spin: 60s @ 0rpm
1.4.6 Water rinse: 15s @ 500rpm; 5000rpm/s
1.4.7 Spin: 40s @2000rpm; 20000rpm/s

Optical Inspection | Comments:

- Defined structures
- Structures' dimensions correct?

STEP 6: *Bottom electrode Definition by Ion Milling* *03/03/2021*

Operator: Maria Carvalho **Machine:** N3600

Etch rates (for reference) 45º: 1.3 Å/s

Sequence name: Etch_stack_45deg

Time steps: 2*170s @ pan = 45°

Extra etching steps (if necessary)

Time steps: 70s + 70s @ pan =45

Conditions:

Base Pressure: ______________ Torr **Run #**3389

Assist Gun	Power (W)	V+ (V)	I+ (mA)	V- (V)	I- (mA)	Ar Flux (sccm)	W.P. (Torr)
Set Point	180	650	-	350	-	16	-
Read Values	180/2	656	104	348	4	16	1.23×10^{-4}

Neutralizer: 0 mA/ 3 sccm

Inspection | Comments

- Oxide color (green/purple)
- No electrical contact (R=∞)
- Burnt resist No
- Profilometry test structure: ΔBE = _____________

STEP 7: Resist Ashing *03/03/2021*

Operator: Maria Carvalho **Machine:** SPTS

Recipe: O2_Ashing_15mTorr_240s

Conditions:

	P_{source} (W)	VP-P_{source} (V)	P_{platen} (W)	VP-P_{platen} (V)	APC (%)	O_2 Flux (sccm)	Pressure (mTorr)	He Press. (Torr)
Set point	600	-	30	-		95	15	15
Read Values	601/2	2526	31/3	260	8.1	95	15	15

Optical Inspection | Profilometry | Comments

- Burnt resist No
- More ashing needed? How much: No
- Step height

STEP 8: *Passivation – SiO_2 Deposition* *03/03/2021*

Operator: _______________ **Machine:** Oxford

Recipe: SiO_2 Deposition

Thickness to deposit: 3000Å **Dep rate:** 70 nm/min

Conditions:

	Total time (min)	Gas flow (sccm)			Temperature (°C)	Source Power (W)
		N_2O	SiH_4	N_2		
Set Point	3 min 50 sec	710	8.5	161.5	300	20
Read Values						

STEP 9: *3rd Lithography – Vias opening* *08/03/2021*

Operator: Maria Carvalho **Machine:** DWL

1.1 Vapor Prime 30 min (Recipe – 0)

1.2 Coat 1.5 µm Photoresist

Recipe Name: 8 resist

1.2.1 Manual resist dispense: 9s @ 800rpm; 10000rpm/s
1.2.2 Spin: 27s @ 2800rpm; 20000rpm/s
1.2.3 Bake 60s @ 95°C

1.3 Lithography

Map: MPW3

Non-Inverted mask

Mask: (\h1 partition)

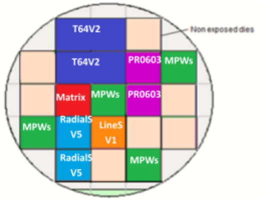

MagID_T64V2_ Via
MagID_RadialS_V5_ Via
MagID_LineS_V1_ Via
PR0603_ Via
MPWs_stat_Via
Matrix_Via

Energy: 95 **Focus:** -10 **Power:** 84

 # Dies: 10 **Total Time:** ~3h 30min

Alignment cross marks: see last page

1.4 Develop

Recipe Name: 8develop

1.4.1 Bake 60s @ 110°C
1.4.2 Water rinse: 5s @ 500rpm; 10000rpm/s
1.4.3 Developer spray: 5s @ 500rpm; 5000rpm/s
1.4.4 Liquid developer: 2.1s @ 0rpm
1.4.5 Spin: 60s @ 0rpm
1.4.6 Water rinse: 15s @ 500rpm; 5000rpm/s
1.4.7 Spin: 40s @2000rpm; 20000rpm/s

Optical Inspection | Comments:

- Defined structures
- Structures dimensions correct?

STEP 10: *Vias opening by Reactive Ion Etching* *09/03/2021*

Operator: Maria Carvalho **Machine:** SPTS

Recipe: SiO2_Vias_etch_ **Etch rate:** 161 nm/min

Thickness to etch: 3000Å **Overetch:** ____%

Conditions:

	P_{source} (W)	VP-P_{source} (V)	P_{platen} (W)	VP-P_{platen} (V)	APC (%)	Gas Flux (sccm)		Pressure (mTorr)	He Press. (Torr)
						CF4	O_2		
Set point	750		100			60	60	12	5
Read Values	750/0	2812	102/7	574	9.5	60	60	12	5

Optical Inspection | Profilometry | Comments:

- Burnt resist No

STEP 11: Resist Ashing *09/03/2021*

Operator: Maria Carvalho **Machine:** SPTS

Recipe: O2_Ashing_15mTorr_240s

Conditions:

	P_{source} (W)	VP-P_{source} (V)	P_{platen} (W)	VP-P_{platen} (V)	APC (%)	O_2 Flux (sccm)	Pressure (mTorr)	He Press. (Torr)
Set point	600	-	30	-		95	15	15
Read Values	601/2	2538	30/4	175	8.1	95	15	15

Optical Inspection | Profilometry | Comments

- Burnt resist No
- More ashing needed? How much: No

STEP 12: Metallization *09/03/2021*

Operator: Maria Carvalho/ Rita Macedo **Machine:** N3600/ N8800

Dep. Rate AlSiCu: 3.0 A/s **Dep. Rate TiWN:** 0.4 A/s

Sequence name: Metalization:

1. Soft etch (60s): Mod 1, F 77
2. AlSiCu 300nm (1000s): Mod 3, F 61, 62, 60 (T5.1 AlSiCu SO 1.8 mTorr)
3. TiWN 15nm (375s): Mod 1, F 75

Base Pressure: _____________ Torr **Run #** 3426

Conditions:

	Assist Gun												
Step	Ar (sccm)	N2 (sccm)	Power (W)	Grid (V)		I (mA)	Gas (sccm)	Power (W)	Grid (V)			I (mA)	W.P (mTorr)
				1	2				1	2	3		
Soft etch	15.9		180	650	380	105							
	15.9		183	657	349	1'05							
AlSiCu 300nm							50	696	495			1400	1.98
							50	683	488			1403	2.03
TiWN 15nm	1	5	160	100	100	23	6	180	1005	275	50	120	1
	1	4.9	133	94	94	24	6.3	145	1008	276	47	120	0.95

Inspection | Comments

STEP 13: *4th Lithography – Top electrode* ___/____/_______

Operator: Maria Carvalho **Machine:** DWL

1.1 Vapor Prime 30 min (Recipe – 0)

1.2 Coat 1.5 µm Photoresist

Recipe Name: 8 resist

1.2.1 Manual resist dispense: 9s @ 800rpm; 10000rpm/s
1.2.2 Spin: 27s @ 2800rpm; 20000rpm/s
1.2.3 Bake 60s @ 95°C

1.3 Lithography

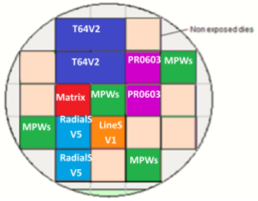

Map: MPW8

Inverted

Mask: (\h1 partition)

MagID_T64V2_ Top
MagID_RadialS_V5_Top
MagID_LineS_V1_ Top
PR0603_ Top
MPWs_stat_Top
Matrix_Top

Energy: 80 **Focus:** -10 **Power:** 84

 # Dies: 14 **Total Time:** _____

Alignment marks: see last page

1.4 Develop

Recipe Name: 8develop

1.4.1 Bake 60s @ 110s
1.4.2 Water rinse: 5s @ 500rpm; 10000rpm/s
1.4.3 Developer spray: 5s @ 500rpm; 5000rpm/s
1.4.4 Liquid developer: 2.1s @ 0rpm
1.4.5 Spin: 60s @ 0rpm
1.4.6 Water rinse: 15s @ 500rpm; 5000rpm/s
1.4.7 Spin: 40s @2000rpm; 20000rpm/s

Optical Inspection | Comments:

- Defined structures
- Structure's dimensions correct?

STEP 14: *Metal etch* *10/03/2021*

Operator: Maria Carvalho **Machine: SPTS**

Recipe: 8inch_Metaletch_60s

Conditions:

	P_{source} (W)	VP-P_{source} (V)	P_{platen} (W)	VP-P_{platen} (V)	APC (%)	Gas flux (sccm)				Pressure (mTorr)	He Press. (Torr)
						BCl_3	Cl_2	HBr	O_2		
Set point	800	-	300	-		10	35	35	1	12	5
Read Values	801 /1	2260	300/ 9	1544	8.9	10	35	35	1	12	5

Optical Inspection | Profilometry | Comments

- Burnt resist: (Resist not removed from LL)
-

STEP 15: Resist Ashing *10/03/2021*

Operator: Maria Carvalho **Machine:** SPTS

Recipe: O2_Ashing_15mTorr_240s

Conditions:

Note: Immerse the wafer in water immediately after removing it from the loadlock.

	P_{source} (W)	VP-P_{source} (V)	P_{platen} (W)	VP-P_{platen} (V)	APC (%)	O_2 Flux (sccm)	Pressure (mTorr)	He Press. (Torr)
Set point	600	-	30	-		95	15	15
Read Values	600/2	2384	31/5	229	8.0	95	15	15

Optical Inspection | Profilometry | Comments

- Burnt resist No
- More ashing needed? How much: No

STEP 16: *Passivation – SiO_2 Deposition* *10/03/2021*

Operator: Eng. Fernando Silva **Machine:** Oxford

Recipe: SiO_2 Deposition

Thickness to deposit: 3000Å **Dep rate:** 78.4 nm/min

Conditions:

	Total time (min)	Gas flow (sccm)			Temperature (°C)	Source Power (W)
		N_2O	SiH_4	N_2		
Set Point		710	8.5	161.5	300	20
Read Values	3 min 50 s					

Optical Inspection | Comments:

STEP 17: 5th *Lithography – Vias opening* *10/03/2021*

Operator: Maria Carvalho **Machine:** DWL

1.1 Vapor Prime 30 min (Recipe – 0)

1.2 Coat 1.5 µm Photoresist

Recipe Name: 8 resist

1.2.4 Manual resist dispense: 9s @ 800rpm; 10000rpm/s
1.2.5 Spin: 27s @ 2800rpm; 20000rpm/s
1.2.6 Bake 60s @ 95°C

1.3 Lithography

Map: MPW8

Non-Inverted mask

Mask: (\h1 partition)

MagID_T64V2_ Pad
MagID_RadialS_V5_Pad
MagID_LineS_V1_ Pad
PR0603_ Pad
MPWs_stat_Pad
Matrix_Pad

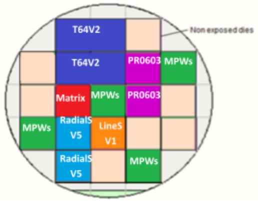

Energy: 80 **Focus:** -10 **Power:** 84

 # Dies: 14 **Total Time:** 4h

Alignment cross marks: see last page

1.4 Develop

Recipe Name: 8develop

1.4.8 Bake 60s @ 110°C
1.4.9 Water rinse: 5s @ 500rpm; 10000rpm/s
1.4.10 Developer spray: 5s @ 500rpm; 5000rpm/s
1.4.11 Liquid developer: 2.1s @ 0rpm
1.4.12 Spin: 60s @ 0rpm
1.4.13 Water rinse: 15s @ 500rpm; 5000rpm/s
1.4.14 Spin: 40s @2000rpm; 20000rpm/s

Optical Inspection | Comments:

- Defined structures
- Structure's dimensions correct?

STEP 18: *Vias opening by Reactive Ion Etching* *11/03/2021*

Operator: Maria Carvalho **Machine:** SPTS

Recipe: SiO2_Vias_etch_1125 **Etch rate:** 161 nm/min

Thickness to etch: 3000Å **Overetch:** ____%

Conditions:

	P_{source} (W)	VP-P_{source} (V)	P_{platen} (W)	VP-P_{platen} (V)	APC (%)	Gas Flux (sccm)		Pressure (mTorr)	He Press. (Torr)
						CF4	O_2		
Set point	750		100			60	60	12	5
Read Values	749/1	2882	103/6	567	9.6	60	60	12	5

Optical Inspection | Profilometry | Comments:

- Burnt resist: (Not removed from LL)

STEP 19: Resist Ashing *11/03/2021*

Operator: Maria Carvalho **Machine:** SPTS

Recipe: O2_Ashing_15mTorr_240s

Conditions:

	P_{source} (W)	VP-P_{source} (V)	P_{platen} (W)	VP-P_{platen} (V)	APC (%)	O_2 Flux (sccm)	Pressure (mTorr)	He Press. (Torr)
Set point	600	-	30	-		95	15	15
Read Values	601/2	2538	30/4	246	8.3	95	15	15

Optical Inspection | Profilometry | Comments

- Burnt resist No
- More ashing needed? How much: No

Note:

Mask	Alignment Marks Coordinates	ΔX, ΔY (μm)
MPWs	L1: [100 ; 100] μm L2: [100 ; 250] μm L3: [100 ; 400] μm L4: [100 ; 550] μm	(2540, 5080)
MagID_T64_V2		
MagID_RadialS_V5		(0, 5080)
MagID_LineS_V1		
PR0603		(2540, 5080) (0, 5080)
Matrix		(0, 1000)

Appendix B

Arduino code

In this appendix, the *Arduino* code for the movement of the 3D precision stage is presented in detail.

B.1 ’.h’ axis library file

Page intentionally left blank.

```
#ifndef MOTORLIBRARY_h
#define MOTORLIBRARY_h

#include "Arduino.h"
#define ENCODER_OPTIMIZE_INTERRUPTS
#include <Encoder.h>

#define REDLED 24
#define BLUELED 23
#define GREENLED 22

struct endStopSwitch{
  int up1;
  int up2;
  int down1;
  int down2;
};

class axis{
  private:
    endStopSwitch switches;
    int encQ1;
    int encQ2;
    int inA1;
    int inA2;
    int axisPWM;
    int setVeloc;

    void ledStatus(int status);

  public:
    long int currentPosition;
    int axisSetSpeed;
    int axisCurSpeed;
    Encoder* axisEnc;
    long int mPos;
    long int pos;
    long int pd;
    int ax;
    int index;

    axis(int encQ1, int encQ2, int inA1, int inA2, int axisPWM, int up1, int up2, uint8_t down1, uint8_t down2);
    void vel(int velocity);
    long int getPosition();
    void goToPosition(long int mPos, int ax);
    void routines(int index);
    double getSpeed();
    void stopAxis();
    int checkEndstops();
    void axisHome(int veloc);
};

#endif
```

B.2 ’.cpp’ axis library file

Page intentionally left blank.

```
#include "Arduino.h"

#include <Encoder.h>
#include "motor_library.h"

//Encoder axisEnc;


axis::axis(int encQ1, int encQ2, int inA1, int inA2, int axisPWM, int up1, int up2, uint8_t down1, uint8_t down2) {
  this->encQ1 = encQ1;
  this->encQ2 = encQ2;
  this->inA1 = inA1;
  this->inA2 = inA2;
  this->axisPWM = axisPWM;
  this->switches.up1 = up1;
  this->switches.up2 = up2;
  this->switches.down1 = down1;
  this->switches.down2 = down2;

  pinMode(switches.up1, INPUT_PULLUP);
  pinMode(switches.up2, OUTPUT);
  pinMode(switches.down1, INPUT_PULLUP);
  pinMode(switches.down2, OUTPUT);

  pinMode(REDLED, OUTPUT);
  pinMode(BLUELED, OUTPUT);
  pinMode(GREENLED, OUTPUT);

  pinMode(inA1, OUTPUT);
  pinMode(inA2, OUTPUT);

  digitalWrite(switches.up2, LOW);
  digitalWrite(switches.down2, LOW);

  //Encoder tempAxis(encQ1, encQ2);
  axisEnc = new Encoder(encQ1, encQ2);// = tempAxis;
  ledStatus(2);
}

void axis::ledStatus(int status) {
  digitalWrite(REDLED, HIGH);
  digitalWrite(BLUELED, HIGH);
  digitalWrite(GREENLED, HIGH);
  if (status == 0)
    digitalWrite(REDLED, LOW);
  if (status == 1) {
    digitalWrite(GREENLED, LOW);
    digitalWrite(REDLED, LOW);
  }
  if (status == 2)
    digitalWrite(GREENLED, LOW);
}

void axis::vel(int velocity) {
  if (velocity == 0) {
    digitalWrite(inA1, LOW);
    digitalWrite(inA2, LOW);
    //curVeloc = velocity;
    //digitalWrite(pinStat, LOW);
    analogWrite(axisPWM, velocity);
    ledStatus(2);
  }
  else if (velocity > 0) {
    //delay(1000);
    digitalWrite(inA1, HIGH);
    digitalWrite(inA2, LOW);
    //curVeloc = velocity;
    //digitalWrite(pinStat, HIGH);
    analogWrite(axisPWM, velocity);
    ledStatus(1);
  }
  else {
    //delay(1000);
    digitalWrite(inA1, LOW);
    digitalWrite(inA2, HIGH);
    //curVeloc = velocity;
    //digitalWrite(pinStat, HIGH);
    analogWrite(axisPWM, -velocity);
    ledStatus(1);
  }
  axisSetSpeed = velocity;
  return;
```

```
}

long int axis::getPosition() {
  long int encPosition = -999;
  encPosition = axisEnc->read();

  return encPosition;
}

void axis::goToPosition(long int mPos, int ax)
{
  long int ip = getPosition();

  //x or y axis
  if (ax == 1 || ax == 2) {
    pos = mPos * 8000 / (2540 * 2);

    if (ax == 1) {
      if (pos > 0) {
        if (mPos > 500) {
          vel(-50);
          while (abs(getPosition()) > abs(0.7 * pos + ip)) {
          }
          vel(-40);
          while (abs(getPosition()) > abs(pos + ip)) {
          }
        }
        else {
          vel(-50);
          while (abs(getPosition()) > abs(0.7 * pos + ip)) {
          }
          vel(-40);
          while (abs(getPosition()) > abs(0.8 * pos + ip)) {
          }
          vel(-37.5);
          while (abs(getPosition()) > abs(pos + ip)) {
          }
        }
      }
      else {
        if (mPos < -500) {
          vel(50);
          while (abs(getPosition()) < abs(0.7 * pos + ip)) {
          }
          vel(40);
          while (abs(getPosition()) < abs(pos + ip)) {
          }
        }
        else {
          vel(50);
          while (abs(getPosition()) < abs(0.7 * pos + ip)) {
          }
          vel(40);
          while (abs(getPosition()) < abs(0.8 * pos + ip)) {
          }
          vel(37.5);
          while (abs(getPosition()) < abs(pos + ip)) {
          }
        }
      }
    }
    else {
      if (pos > 0) {
        if (mPos > 500) {
          vel(-42.5);
          while (abs(getPosition()) > abs(0.8 * pos + ip)) {
          }
          vel(-35);
          while (abs(getPosition()) > abs(pos + ip)) {
          }
        }
        else {
          vel(-42.5);
          while (abs(getPosition()) > abs(0.6 * pos + ip)) {
          }
          vel(-35);
          while (abs(getPosition()) > abs(0.7 * pos + ip)) {
          }
          vel(-27.5);
          while (abs(getPosition()) > abs(0.8*pos + ip)) {
          }
          vel(-25);
```

```
        while (abs(getPosition()) > abs(pos + ip)) {
        }
      }
    }
    else {
      if (mPos < -500) {
        vel(42.5);
        while (abs(getPosition()) < abs(0.7 * pos + ip)) {
        }
        vel(35);
        while (abs(getPosition()) < abs(pos + ip)) {
        }
      }
      else {
        vel(42.5);
        while (abs(getPosition()) < abs(0.6 * pos + ip)) {
        }
        vel(35);
        while (abs(getPosition()) < abs(0.7 * pos + ip)) {
        }
        vel(27.5);
        while (abs(getPosition()) < abs(0.8*pos + ip)) {
        }
        vel(25);
        while (abs(getPosition()) < abs(pos + ip)) {
        }
      }
    }
  }
  vel(0);
  delay(1000);
  Serial.println((double)(abs(ip - getPosition()) * 2540 / 4000));
}
//z axis
else {
  pos = mPos * 8000 / 2000;
  if (pos > 0) {
    if (mPos > 500)
    {
      vel(30);
      while (abs(getPosition()) < abs(0.7 * pos + ip)) {
      }
      vel(20);
      while (abs(getPosition()) < abs(0.8 * pos + ip)) {
      }
      vel(17.5);
      while (abs(getPosition()) < abs(0.9 * pos + ip)) {
      }
      vel(15);
      while (abs(getPosition()) < abs(pos + ip)) {
      }
      vel(0);
    }
    else if (mPos >= 20 && mPos <= 500) {
      vel(15);
      while ((double)abs(getPosition()) < (double)abs(0.7 * pos + ip)) {
      }

      vel(13.5);
      while ((double)abs(getPosition()) < (double)abs(0.8 * pos + ip)) {
      }
      vel(12);
      while ((double)abs(getPosition()) < (double)abs(pos + ip)) {
      }
      vel(0);
    }
    else {
      vel(11);
      while ((double)abs(getPosition()) < (double)abs(0.75 * pos + ip)) {
      }
      vel(10);
      while ((double)abs(getPosition()) < (double)abs(0.8 * pos + ip)) {
      }
      vel(9);
      while ((double)abs(getPosition()) < (double)abs(pos + ip)) {
      }
      vel(0);
    }
  }
  else {

    if (mPos < -500)
```

```
      {
        vel(-30);
        while (abs(getPosition()) > abs(0.7 * pos + ip)) {
        }
        vel(-20);
        while (abs(getPosition()) > abs(0.8 * pos + ip)) {
        }
        vel(-17);
        while (abs(getPosition()) > abs(0.9 * pos + ip)) {
        }
        vel(-15);
        while (abs(getPosition()) > abs(pos + ip)) {
        }
        vel(0);
      }
      else if (mPos <= -20 && mPos >= -500) {
        vel(-15);
        while ((double)abs(getPosition()) > (double)abs(0.7 * pos + ip)) {
        }
        vel(-13.5);
        while ((double)abs(getPosition()) > (double)abs(0.8 * pos + ip)) {
        }
        vel(-12);
        while ((double)abs(getPosition()) > (double)abs(pos + ip)) {
        }
        vel(0);
      }
      else {
        vel(-11);
        while ((double)abs(getPosition()) > (double)abs(0.75 * pos + ip)) {
        }
        vel(-10);
        while ((double)abs(getPosition()) > (double)abs(0.8 * pos + ip)) {
        }
        vel(-9);
        while ((double)abs(getPosition()) > (double)abs(pos + ip)) {
        }
        vel(0);
      }
    }
    delay(1000);
    Serial.println((double)abs(ip - getPosition()) * 2000 / 8000, 4);
  }
}

void axis::routines(int index){
  //Z axis routine: move 20 times, 100um
  if(index == 1){
    for(int i=0;i<10;i++)
    {
      goToPosition(32,3);
      //delay(1000);
    }
  }
  else if(index == 2){
    for(int i=0;i<20;i++)
    {
      goToPosition(100,1);
      Serial.println(i);
      Serial.println(getPosition());
    }
  }
}

//double axis::getSpeed(){
//  int pos1 = getPosition();
//  int t1 = millis();
//  delay(1);
//  int pos2 = getPosition();
//  int t2 = millis();
//
//  return (double)(pos2-pos1)/(double)(t2-t1);
//}

void axis::stopAxis() {
  vel(0);
  return;
}

int axis::checkEndstops() {
  if (digitalRead(switches.up1)) {
    //ledStatus(2);
```

```
    return 1;
  }
  else if (digitalRead(switches.down1)) {
    //ledStatus(2);
    return -1;
  }
  else
    return 0;
}

void axis::axisHome(int velocity) {
  vel(-velocity);
  while (checkEndstops() == 0) { //o axis move-se enquanto não chega ao endstop
    //Serial.println(getPosition());
  }
  vel(0);
  delay(100);
  axisEnc->write(0);
  currentPosition = 0;
  long int p1 = 0;
  //Serial.println(p1);
  //delay(5000);

  vel(velocity);
  delay(100);
  while (checkEndstops() == 0) {
    //Serial.println(getPosition());
  }
  vel(0);
  delay(100);
  long int p2 = getPosition();
  //Serial.println(p2);
  //delay(5000);

  vel(-velocity);
  //Serial.println(getPosition());
  //  long int pd = (p2 - p1)/(long int)2;
  pd = (p2 - p1) / (long int)2;
//  Serial.println(p1);
//  Serial.println(p2);
//  Serial.println(pd);
  delay(100);
  while (abs(getPosition() - pd) > 1000) {

    //Serial.println(getPosition());
  }
  vel(0);

}
```

B.3 ’.cpp’ implementation file

Page intentionally left blank.

```
//#define ENCODER_OPTIMIZE_INTERRUPTS

#include <Encoder.h>
#include "motor_library.h"

axis xAxis(18, 19, 4, 5, 10, 49, 47, 48, 46);
axis yAxis(2, 3, 6, 7, 11, 52, 50, 53, 51);
axis zAxis(20, 21, 8, 9, 12, 45, 43, 44, 42);

int input = 0;
long int ip;
long int pos = 0;
long int pos2 = 0;
const unsigned int MAX_LENGTH = 12;

void setup() {
  //Other definitions
  TCCR1B = TCCR1B & B11111000 | B00000001;
  TCCR2B = TCCR2B & B11111000 | B00000001;
  //pinMode(pinStat, OUTPUT);

  Serial.begin(9600);
  delay(1000);
  //
  while (Serial.available() < 1);
  xAxis.axisHome(80);
  yAxis.axisHome(60);
  zAxis.axisHome(30);
  delay(1000);
}


void loop() {
  // fade in from min to max in increments of 5 points:

  if (Serial.available() > 1) {
    //Serial.print("READY")

    pos2 = Serial.parseInt();
    pos = Serial.parseInt();

}
else {
  if (xAxis.checkEndstops() == 1) {
    Serial.println("ENDSTOP DOWN");
    if (pos > 0)
      xAxis.vel(0);
    if (pos < 0)
      return;
  }
  else if (xAxis.checkEndstops() == -1) {
    Serial.println("ENDSTOP UP");
    if (pos < 0)
      xAxis.vel(0);
    if (pos > 0)
      return;
  }
  //Serial.println(xAxis.getPosition());
  //Serial.println(xAxis.getSpeed());
  //Serial.println("READY");
  return;
}
```

```
//Serial.println(pos);
//Serial.println(pos2);

if ( pos2 == 1 && pos == 0){
  //Serial.println("home");
   xAxis.axisHome(80);
  yAxis.axisHome(60);
  zAxis.axisHome(30);
}
else if (pos == 0) {
  //Serial.println("STOP");
  xAxis.vel(input);
}
else if ( pos2 == 1){
    //Serial.println("Position x");
    xAxis.goToPosition(pos, 1);
  }
else if ( pos2 == 2){
  //Serial.println("Position y");
  yAxis.goToPosition(pos, 2);
}
else if ( pos2 == 3){
      //Serial.println("position z");
      zAxis.goToPosition(pos, 3);
}
//else if (pos2 == 4){
//    //Serial.println("routines");
//    if(pos == 1) zAxis.routines(1);
////    if(pos == 2) xAxis.routines(2);
//}
}
```

Appendix C

Precision Movement Stage's electrical connections

Page intentionally left blank.

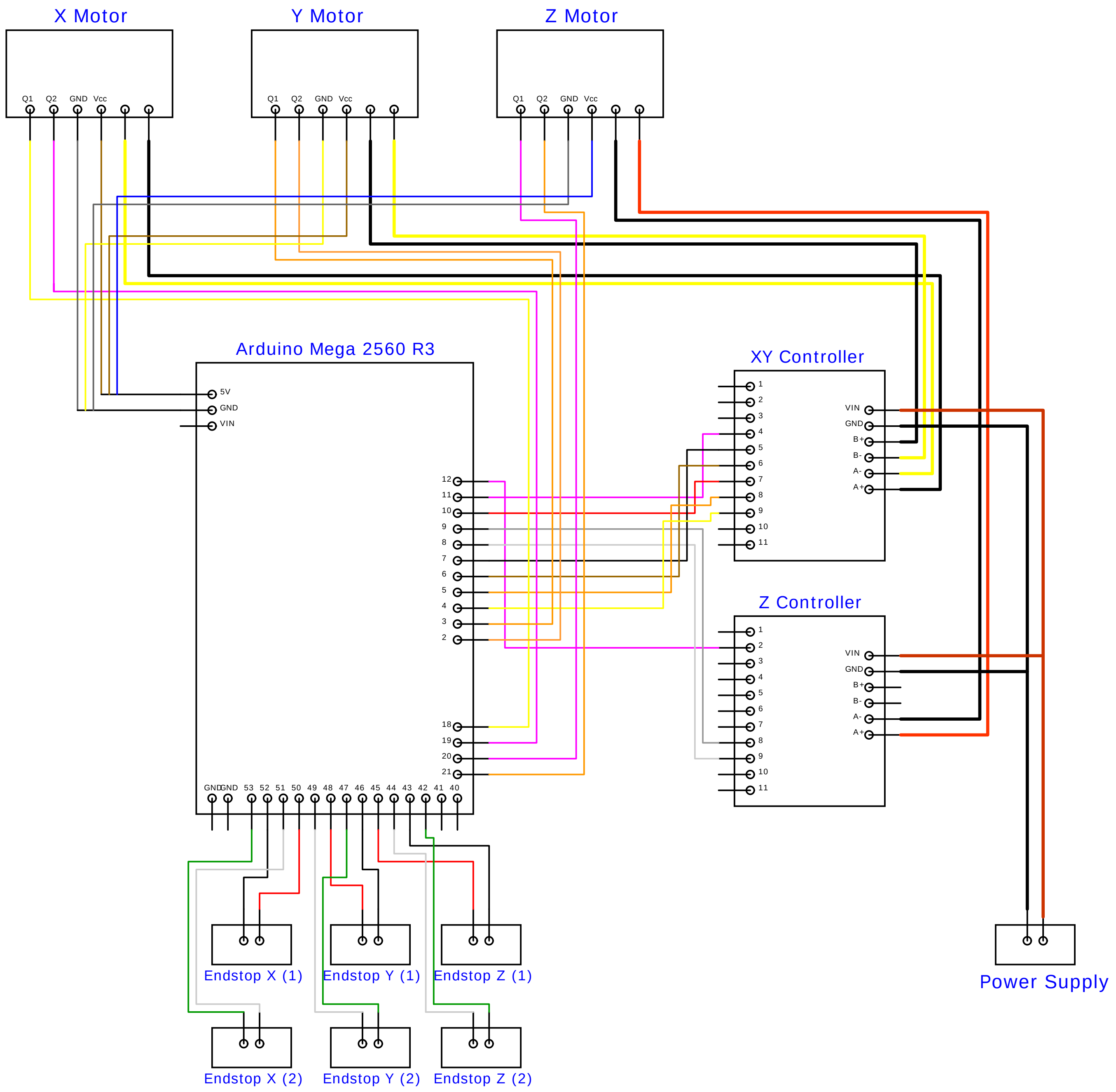

TITLE: Eletrical Scheme: Precise measurement setup

REV: 1.0

Company:

Sheet: 1/1

Date: 2021-09-30

Drawn By: ritapagaimo

Appendix D

Data acquisition board hardware schematics

Page intentionally left blank.

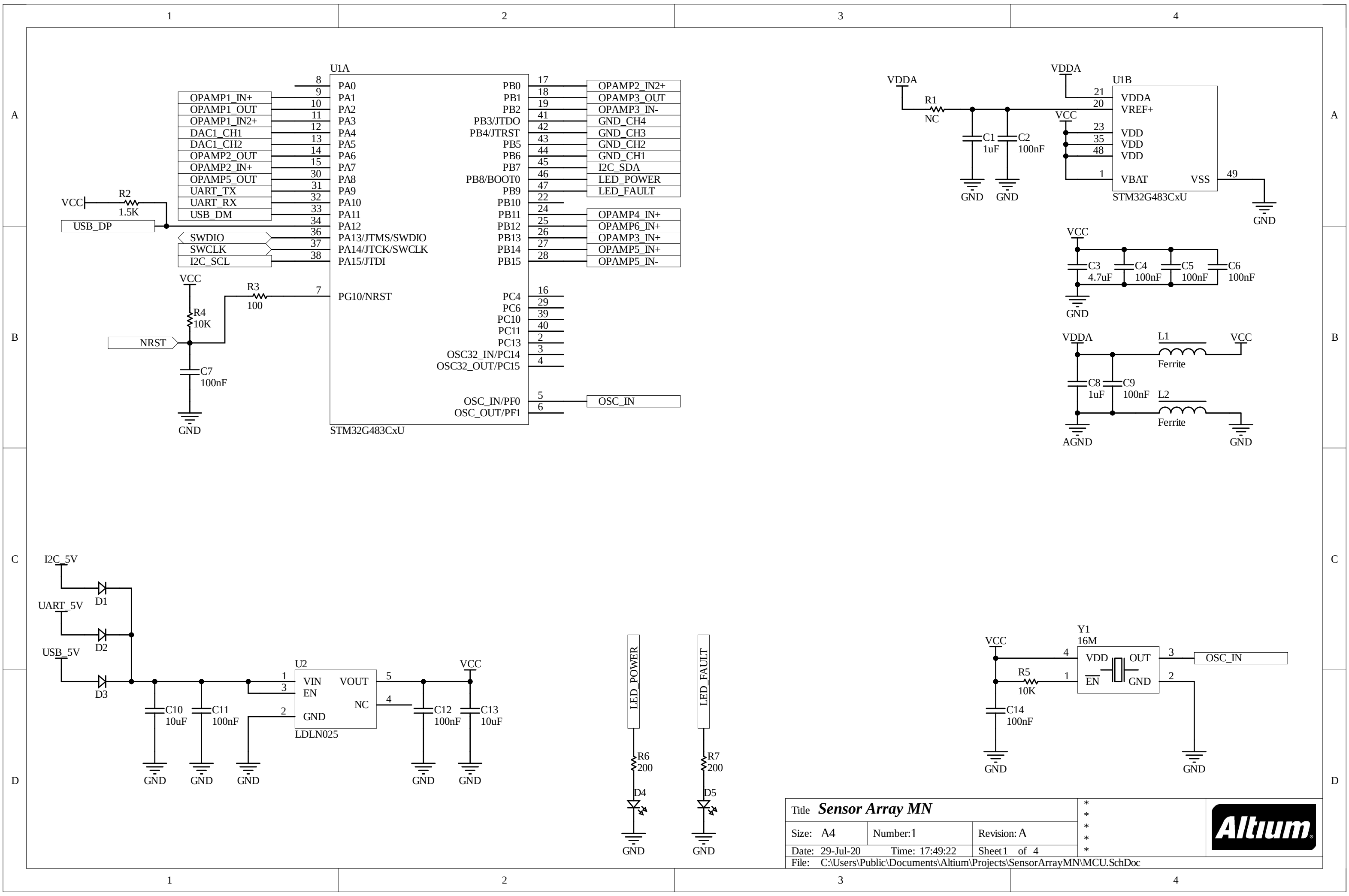

Title **Sensor Array MN**

Size: A4 Number:1 Revision: A

Date: 29-Jul-20 Time: 17:49:22 Sheet 1 of 4

File: C:\Users\Public\Documents\Altium\Projects\SensorArrayMN\MCU.SchDoc

Altium

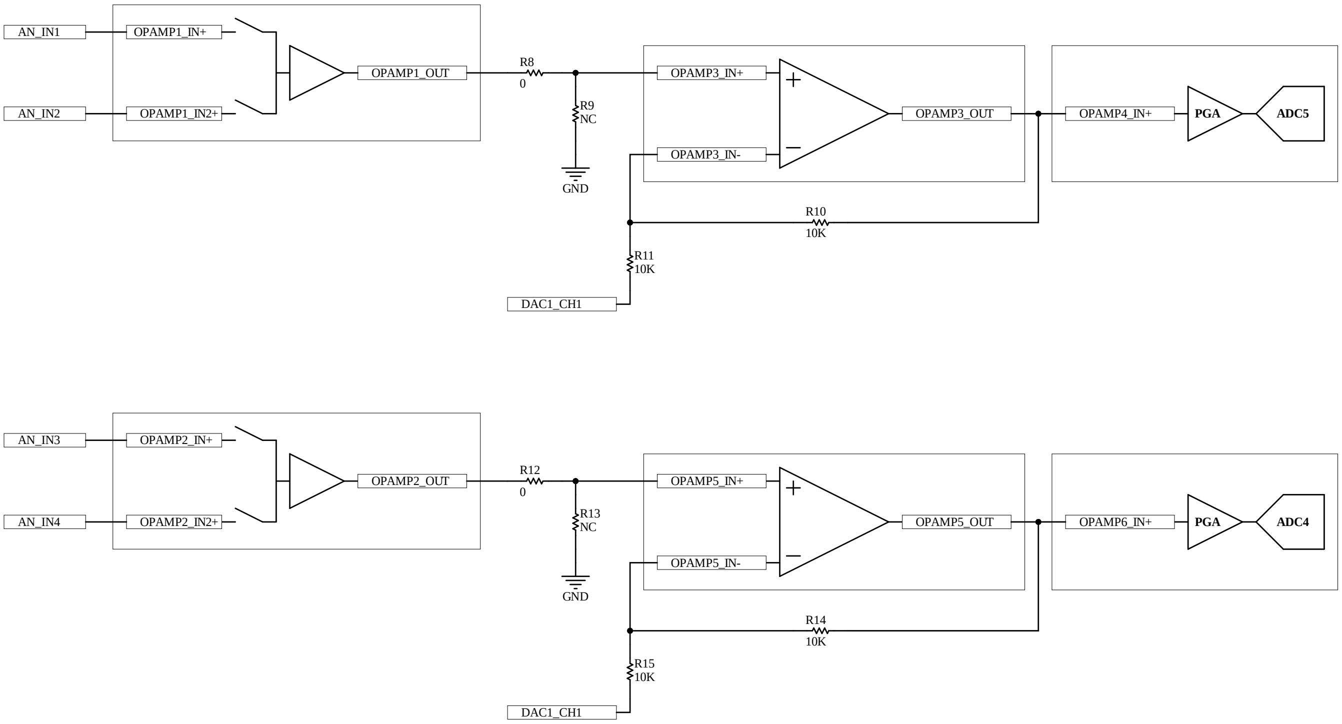

Title *Sensor Array MN*

Size: A4 Number:2 Revision: A

Date: 29-Jul-20 Time: 17:49:22 Sheet 2 of 4

File: C:\Users\Public\Documents\Altium\Projects\SensorArrayMN\AnalogIn.SchDoc

*
*
*
*
*

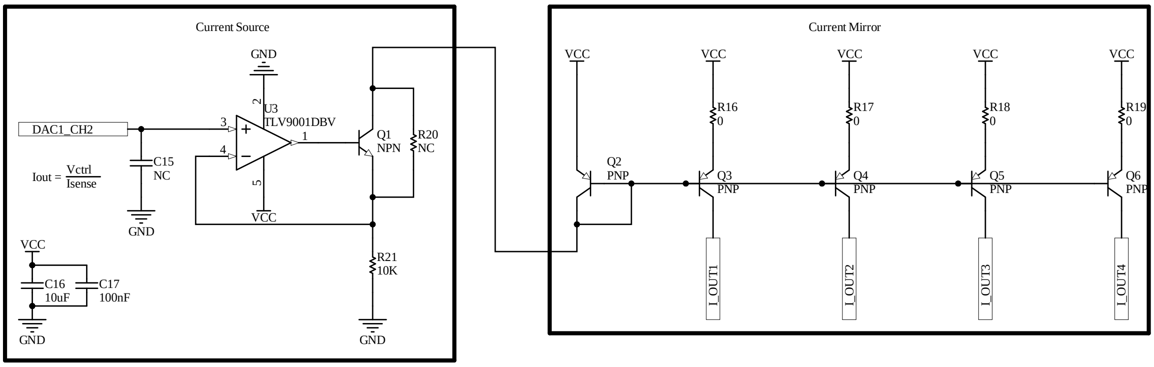

Title **Sensor Array MN**

Size: A4 Number: 3 Revision: A

Date: 29-Jul-20 Time: 17:49:22 Sheet 3 of 4

File: C:\Users\Public\Documents\Altium\Projects\SensorArrayMN\CurrentSource.SchDoc

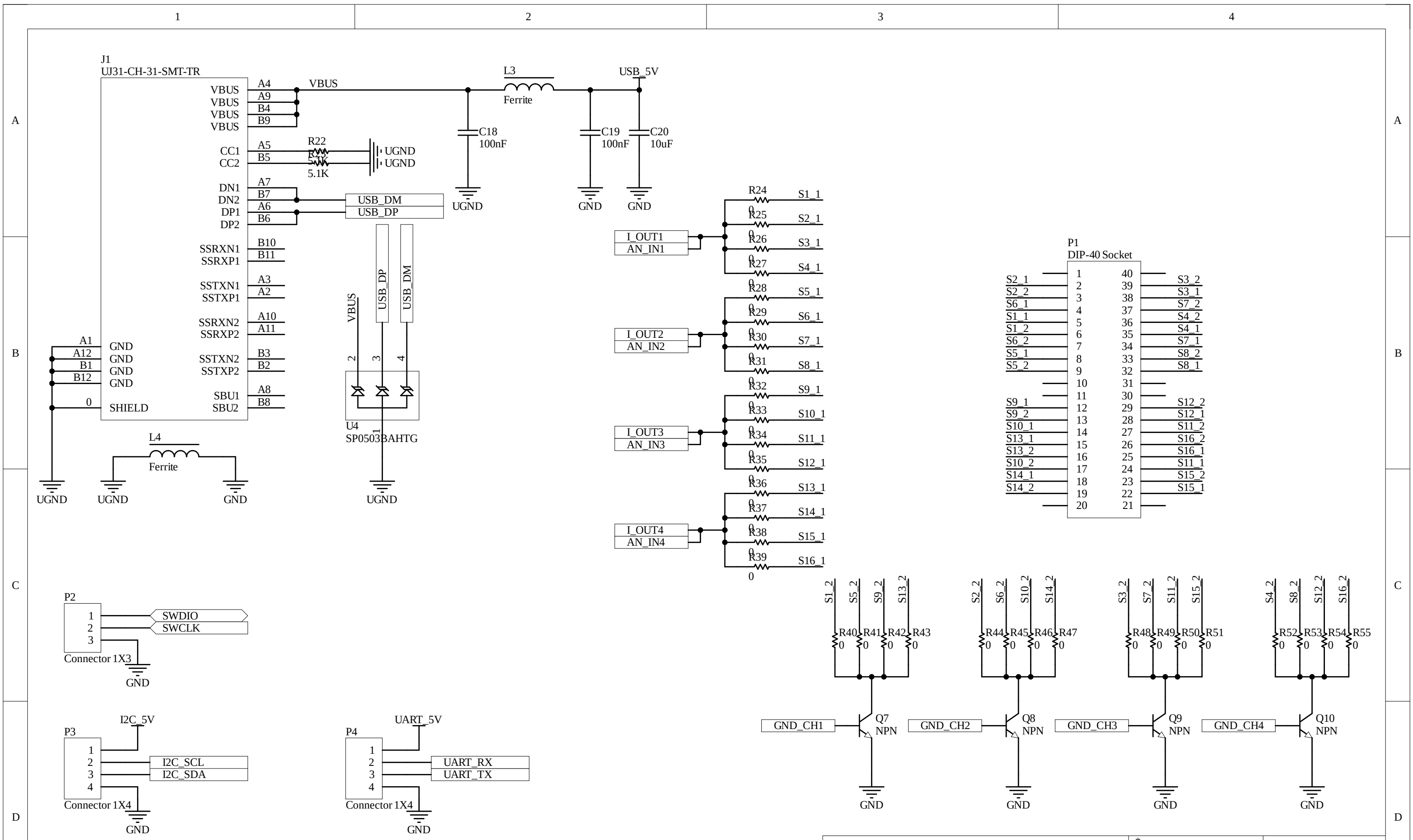

Title	*Sensor Array MN*		
Size: A4	Number:4		Revision: A
Date: 29-Jul-20	Time: 17:49:22		Sheet 4 of 4
File: C:\Users\Public\Documents\Altium\Projects\SensorArrayMN\Connector.SchDoc			

*
*
*
*
*